Full field-of-view virtual reality goggles for mice

Domonkos Pinke[1,3], John B. Issa[1,3], Gabriel A. Dara[1], Gergely Dobos[2], Daniel A. Dombeck[1,4,*]

[1] Department of Neurobiology, Northwestern University, Evanston, IL, 60208, USA
[2]360world Ltd, Budapest, Sümegvár köz 9. 1118, Hungary
[3]These authors contributed equally.
[4] Lead contact
[*] Correspondence: d-dombeck@northwestern.edu

Summary

Visual virtual reality (VR) systems for head-fixed mice offer advantages over real-world studies for investigating the neural circuitry underlying behavior. However, current VR approaches do not fully cover the visual field-of-view of mice, do not stereoscopically illuminate the binocular zone, and leave the lab-frame visible. To overcome these limitations, we developed iMRSIV (Miniature Rodent Stereo Illumination VR)—virtual reality goggles for mice. Our system is compact, separately illuminates each eye for stereo vision and provides each eye with an ~180-degree field-of-view, thus excluding the lab frame while accommodating saccades. Mice navigating using iMRSIV engaged in virtual behaviors more quickly than in a current monitor-based system and displayed freezing and fleeing reactions to overhead looming stimulation. Using iMRSIV with two-photon functional imaging, we found large populations of hippocampal place cells during virtual navigation, global remapping during environment changes, and unique responses of place cell ensembles to overhead looming stimulation.

Introduction

The mechanical stability provided by mouse head-fixation has facilitated the use of high-resolution functional microscopy[1-4], intracellular patch clamp recording[5-8] and large-scale single unit recording in behaving mice[9,10] that are either stationary or running on treadmills. The addition of visual virtual reality (VR) simulations, driven in closed loop by treadmill movements, has provided the ability to study spatial behaviors in head-fixed mice[11-13]. These systems have been used to investigate neural circuits underlying behaviors such as goal-directed navigation, decision making, accumulation of evidence and path integration[14-17]. However, despite these advantages, current VR approaches have limitations that potentially reduce rodent immersion in the virtual environment.

Proper illumination of the mouse visual system is particularly challenging due to the wide field of view (FOV) of the mouse eye. Each mouse eye accepts a FOV of ~140-degrees (both in the azimuthal and vertical elevation directions), with ~40 degrees of binocular overlap in the azimuthal plane and more at larger vertical elevations at the resting eye position, leading to a full azimuthal FOV of ~240 degrees and vertical elevation FOV >~200 degrees[18-20] (Figure 1A-B). Current VR (VR) systems typically consist of a head-fixed mouse running on a treadmill with a surrounding visual display consisting of either a large, curved screen illuminated by a projector or multiple computer monitors assembled side-by-side. Projection systems typically illuminate ~270 and 160 degrees of the azimuthal and vertical elevation[13], and monitor based systems ~220 and 140 degrees[21], leaving portions of the mouse FOV un-illuminated, particularly in the vertical elevation direction in the critical overhead region[22,23] (Figure 1C). Additionally, in the distance between the mouse and VR screens in current systems (0.5-1m), objects in the lab frame are visible (head-fixation bars, optical table-top, lick tube, screen bezels, cameras, etc.). Importantly, the microscope itself is within (and blocking) the overhead field-of-view of the mouse. These immobile objects do not move with the virtual simulation and therefore provide cue-conflicts between the virtual and lab reference frames while also partially blocking views of the virtual world.

Another important and unique feature of the mouse visual system is the large binocular region that mice maintain both to the front and, even more prominently, above their head (Figure 1A). Because of the separation of the eyes on the animal's head, real-world objects in the binocular FOV region are viewed by each eye at different angles (binocular disparity). The overhead visual region is particularly important for rodent behavior and survival, as mice continually monitor binocular overlap for threats coming from above[22] (Figure 1B). Current VR systems generate a single rendering of the virtual world so that each eye sees the same view of objects in the binocular region, eliminating stereo depth information that may be present (Figure 1C). Furthermore, as mentioned, recording components (such as an upright microscope) and head fixation bars occlude the overhead visual region. Overall, the above limitations lead to deviations in how the visual system is illuminated between real and virtual environments[24,25] and may reduce the overall immersion of current rodent VR systems.

Lastly, current VR systems are relatively large and often require significant engineering for the inclusion of microscopy or electrophysiology components. Their large size may also be prohibitive for building large scale behavior training arrays, where dozens of mice can be trained on relatively complicated tasks at the same time[26,27].

We therefore developed a mouse VR goggle system (Figure 1D) where the lab frame is not visible and each mouse eye is separately illuminated, providing a full FOV (with additional FOV for saccades, Figure S1)

and stereo illumination to the binocular visual zone, including the critical overhead region. We validate our optical design using optics simulations and real-world measures of retina illumination. We then demonstrate the usefulness of our small footprint iMRSIV (Miniature Rodent Stereo Illumination VR) system by training mice in a virtual navigation task and compare their task engagement to a conventional VR system. We demonstrate that mice displayed dramatic freezing and fleeing reactions to looming stimulation of the overhead binocular zone, a behavioral response that was not observed in the conventional VR system. Additionally, we performed two-photon functional imaging of CA1 populations during these tasks and demonstrate that our system activates large populations of place cells during linear track navigation and global remapping during a track switch paradigm. Finally, in an experiment made uniquely possible with our system, we recorded place cell firing patterns before, during and after overhead looming stimulation and discover previously unknown place cell remapping and remote encoding patterns.

Results

iMRSIV goggle device design and validation

To facilitate the design and testing of the optics of our iMRSIV system, we began with existing Zemax models of the mouse eye[28,29] and examined the image generated on the simulated eye retina by a 482x261mm checkerboard object at a distance of 200mm (Figure 2A,B,D). We reproduced this arrangement in the real-world by generating the same size and distance checkerboard pattern on a computer monitor and examined the resulting image of the object on the retina of an extracted mouse eye (Figure 2C,E). We then made minor modifications to the Zemax mouse eye model to obtain highly similar retinal illumination patterns between the real-world experiments and simulations (Figure 2D,E; Figure S2A,F-H), thus obtaining a simulation environment to design and test our iMRSIV system.

We were able to test many optical designs to achieve our goal of illuminating each mouse eye with a ~180-degree FOV in all directions (140 degrees for each eye FOV +/-20 degrees for saccades), which we aimed to achieve with a single screen and single lens per eye (Figure 2F). It was not possible to realize a 180-degree FOV with a plano-convex or bi-convex lens. Instead, a positive-meniscus lens was required so that each mouse eye could be fully enveloped. We arrived at a unique optical system that achieved a ~180-degree FOV by using a custom designed positive-meniscus lens paired with a small curved illumination display (Figure 2G,H).

We then asked whether, in a Zemax simulation, we could reproduce the above checkerboard illumination of the mouse retina using our small display and lens combination. We first needed to compensate for distortions introduced by our optical element, so we used Unity3D to recreate the checkerboard arrangement in a virtual world simulation (482x261mm checkerboard object at a 200mm distance) and generated a 180-degree FOV of this scene using a single Unity3D camera and a custom fish-eye shader (Figure 2I). Not only did the fish-eye shader provide for a 180-degree FOV, but it also compensated well for the distortions of our custom lens (Figure S3A). This 180-degree FOV was displayed on the small, curved display in Zemax and used as the object so we could examine the resulting image (through the positive-meniscus lens) on the simulated mouse eye retina, which was centered at a 1mm distance from the inner surface of the lens. We found that the resulting simulated retina image of the checkerboard pattern (Figure 2L; 140 of the available 180-degree FOV) was highly similar to both the Zemax model of the checkerboard object (Figure 2D) and the real-world arrangement of this scene using a computer monitor and extracted mouse eye (Figure 2E; Figure S2A-E).

We then fabricated our optical system for real-world use and validation. The lens was custom ground (Shanghai-Optics) and a small, flexible, round OLED screen (1.39 in diameter, 400x400 pixel, Innolux) was used for the display. The final assembly consisted of two separate 3D printed parts held together with magnets: first, a screen-holder with a curvature matching that of our simulations, to which the OLED screen was affixed; second, a cone-shaped lens-holder with the lens glued to one end and the other end mated to the screen-holder with magnets such that the lens was centered at the desired distance from the screen (6.3mm; Figure 2K). Across a 180-degree FOV, our system provided a mean resolution of 2.2 pixels/degree, higher than the 0.375 cycles/degree visual acuity estimated for the C57BL6 mouse strain used for behavior and imaging experiments here[30].

We then asked whether, using our real optical system, we could reproduce the above checkerboard illumination of the mouse retina. We used the Unity3D virtual checkerboard arrangement (482x261mm

checkerboard object at a 200mm distance) and fisheye shader to generate a 180-degree view of this scene (from Figure 2I) and illuminated the real OLED screen with this view. We then examined the resulting image of the checkerboard object on the retina of an extracted mouse eye, centered at a 1mm distance from the inner surface of the positive-meniscus lens (Figure 2M). We found that the resulting retina image of the checkerboard pattern (Figure 2M; 140 of the available 180-degree FOV) was highly similar to both the Zemax models of the checkerboard object (Figure 2L; Figure S2I-K) and the real-world arrangement of this scene using a computer monitor (Figure 2E; Figure S2F-K). Finally, we simulated a 20-degree saccade using both Zemax simulations and real-world extracted mouse eye experiments (Figure 2J,N,O). We found highly similar retina images of the checkerboard pattern in both cases (Figure 2N,O; Figure S2L-Q and Videos S1-2). Thus, we established and validated an optical system able to illuminate a ~180-degree FOV for the mouse eye—140-degree FOV +/-20-degrees in each direction for saccades.

The small OLED screen, custom positive-meniscus lens and 3D printed parts make up one half (one eye) of our mouse VR goggle system; a duplicate assembly was therefore made for the other eye. Unity3D cameras were used to generate the ~180-degree FOV for each display for each eye. For proper placement of the Unity3D cameras, we used a virtual mouse and placed one camera at each eye, with the camera angles with respect to the mouse set at the resting eye position (22-degrees vertical elevation from the lambda-bregma plane and 64-degrees azimuth from the midline)[31]. This arrangement ensured proper views of the virtual world for each eye and, because of the different position of the cameras in Unity 3D, each one created a different view of objects in the binocular region, thus providing stereoscopic information to the mouse. Together, these components, the renderings of the virtual world for each eye and the custom Unity3D shader complete our goggle system, which we refer to as the iMRSIV (Miniature Rodent Stereo Illumination VR) system.

iMRSIV behavior apparatus and device-eye alignment procedures

To use the iMRSIV system with head-fixed mice running on a treadmill, we added a cylindrical treadmill, water reward delivery system, capacitive lick sensor, fixed head-plate mounting posts to hold the head-plate at the same location for each mouse in each session, structural components to hold each half of the iMRSIV system in place and two 3D micromanipulators for alignment of the iMRSIV system (Figure 3A,B). We modified Unity3D to communicate with a National Instruments DAQ card (PCIe-6323) and used a digital output signal from this card to control a solenoid for water rewards, a digital input for lick sensor monitoring, and a quadrature encoder input to read treadmill velocity from a rotary encoder (Figure 3C).

Our Zemax simulations and extracted eye experiments highlighted the need for precise alignment and positioning of the iMRSIV system lenses relative to the eyes of the mouse (Figure S4). For angular alignment, the manipulators and structural components were designed to align the iMRSIV system optical axis with the optical axis of the mouse eye at its resting position (22-degrees vertical elevation from the lambda-bregma plane and 64-degrees azimuth from the midline)[31], which matched the angles used for the virtual cameras in Unity3D. With the angle set, proper positioning then required each eye to be centered 1mm from the inner surface of each positive-meniscus lens. To achieve this position, we used two steps. First, during the surgery, we used a 3D-printed frame to implant a head-plate at the same location with respect to the eyes across different mice (Figure 3D, Methods). This frame included indicator targets, which, when aligned to the center of the mouse eyes, specified the correct head-plate implantation location. These surgical methods greatly reduced mouse-to-mouse and session-to-session variability in the location of the eyes with respect to the head-plate, and therefore with respect to the iMRSIV system (further details on the procedure and quantification of expected variability are provided under "iMRSIV alignment procedures" in Methods). Second, for final positioning of each mouse at the start of each behavioral session, mice were head-fixed using the mounting posts and then a 3D printed frame was used to position each half of the iMRSIV system with respect to each eye (Figure 3E). The conical lens-holder was removed from each half (pulled off from magnetic attachment) and replaced with a frame with an eye target, which was aligned to each eye using the micropositioners. Once aligned, the target was again replaced with the conical lens-holder, which was now in the correct position with the eye centered at a 1mm distance from the lens (Figure 3F).

iMRSIV spatial behaviors: linear track and looming stimulation

We next sought to determine whether mice could learn to perform a virtual linear track task[1,13,32] where mice navigated a linear track to a fixed reward location; trained mice in such tasks develop behaviors indicative of anticipation of the reward location. We trained 7 water-scheduled mice to run along a 3-meter virtual linear track (Figure 4A). The mice started in a tunnel, ran across an open field, received a 3 μL water reward near the end of the field, entered a tunnel and were then teleported back to the track start for another trial. For comparison, we also trained 13 separate water-scheduled mice on the same task but using a conventional VR system consisting of 5 computer monitors mounted side-by-side. All aspects of the environments, training and mice were the same between the groups, with the only difference being the type of visual display rendering the simulations (iMRSIV vs 5 panel). We found that three mice in the iMRSIV group ran more than 0.5 trials per minute over the first ~45-minute sessions (iMRSIV group mean of 0.79+/-1.40 trial/minute in first session), and on average mice in this group reached expert levels (3.21+/-1.80 trials/minute) after ~6 days of training (Figure 4B). Only 1 mouse in the 5-panel group ran more than 0.5 trials per minute in the first session, and on average mice in this group reached expert levels at a similar number of days of training as the iMRSIV group (5-panel group mean of 0.13+/-0.16 trials/minute on day 1 and 2.75+/-1.88 trials/minute on day 6; no significant difference in trials/minute between groups, $p > 0.05$, 2-sample t-test).

We then examined anticipatory licking behavior in the different groups across days (Figure 4C), since this measure has previously been used to assess behavioral learning and task engagement[33-35] in linear tracks. Importantly, we found that on the first day of training the iMRSIV group displayed significantly more anticipatory licking than the 5-panel group. This was quantified by calculating a pre-licking index to determine the fraction of licking (excluding consumptive licking) that occurred just before the reward compared to other track locations (day 1: iMRSIV group pre-lick index = 0.64+/-0.24, 5-panel group pre-lick index 0.06+/-0.11; 2-sample t-test, $p=0.0004$). Over 4-6 days, mice in both groups displayed similar pre-licking indices, with most non-consumptive licking occurring just before the reward location. Therefore, mice engaged in a virtual navigation behavior more quickly using the iMRSIV system compared to the existing monitor-based VR system and refined their licking behavior to become highly precise and location specific after several days of training.

To take advantage of the unique access the iMRSIV system provides to illuminate the overhead visual scene, we sought to reproduce freezing and fleeing behaviors observed during real-world open field looming stimulation of the overhead region[23,36,37]. After mice were trained on the first linear track (Figure 4A) for at least 6 days (~2-3 rewards/minute), they were switched to a new linear track with the same tunnels at the ends, but an open field in the middle with few cues (Figure 4D). Once this track became familiar (2-3 sessions), we introduced a single, sudden overhead looming stimulus (overhead increasing size sphere, with shadow over the mouse) in the middle of a behavior session when the mice were in the center of the open field (Figure 4D). The iMRSIV group mice displayed a dramatic reaction (Figure 4E; Figure S5A-C). All mice froze after the stimulus (mean freezing time until first detected movement after the first looming stimulus in each mouse: 3.95+/-4.4 minutes): 3 of 7 mice froze immediately at the start of the looming stimulus, while 4 of 7 mice rapidly accelerated for several seconds (fleeing behavior) before freezing. When mice began running down the track again after freezing, their running velocity was slower than before (26.7+/-11.4 cm/s in the minute before loom vs 11.6+/-6.6 cm/s in the minute after freezing; paired t-test, $p=0.043$). The same stimulus was applied to a subset of the 5-panel group mice but, due to the lack of overhead illumination, the mice were unable to see the looming sphere and could only see its shadow. This lack of overhead illumination is typical for current VR systems, and even though an overhead monitor could be added any current VR system, it would be occluded by overhead recording equipment (Figure 1C) and, further, would not generate a stereoscopic view. We therefore used the 5-panel group mice as a control for a reaction to the shadow. The 5-panel mice did not respond to the shadow (or stimulus), they displayed no acute freezing or acceleration/deceleration and their running speed before and after the stimulus was not different (21.4+/-10.8 cm/s in the minute before loom vs 22.5+/-9.0 cm/s in the minute after loom; paired t-test, $p=0.53$). Therefore, the iMRSIV system provides experimental control of the overhead visual scene, which can be used to provide looming stimulation to head-fixed mice, leading to dramatic freezing responses that last for minutes.

Two-photon calcium imaging during iMRSIV spatial behaviors

Typically, microscopy systems occlude the overhead space above head-fixed mice (Figure 1C). However, the design of the iMRSIV system allowed us to place it under an upright two-photon microscope, providing a full FOV, including the overhead region, while imaging (Figure S5D-F and Video S3). To block light from the illuminated screens from being detected by the microscope's photodetectors, we designed custom shielding that fit around the objective and connected to a ring on the head of the mouse. Four out of the seven iMRSIV behavior group mice were injected with a virus to induce expression of jGCaMP8m in CA1 of the dorsal hippocampus and were implanted with a chronic hippocampal imaging window[12] (Figure 5A); these four mice were used for the subsequent imaging experiments.

After at least 6 days of training, two-photon imaging was performed to record CA1 neural activity while mice performed the linear track task (8 imaging sessions from 4 mice, 4 familiar track sessions, 4 environment switch sessions; 450x450 μm field size, 30.28 frames/sec, 28.7 minutes/imaging session, 297+/-95 neurons segmented/field). In a familiar linear track, we identified many place cells (204+/-61 place cells per field, 69.4+/-8.8% of active cells had significant place fields), and these place cells were highly reliable, with most cells active on the majority of trials (mean reliability: 0.51+/-0.14; Figure S5G). These cells tiled the linear track on single trials but with a significantly larger number of place fields near the reward zone[11,32,38-40] (Figure 5B). We also performed imaging of CA1 neural activity in mice trained using the 5-panel displays instead of iMRSIV. Results were similar for CA1 place cells in the 5-panel group (Figure S5H-I).

Next, in the middle of a familiar track session, we suddenly switched mice into a novel environment that they had not seen before. We found that many familiar place cells did not have place fields in the novel environment (44+/-12%). The cells that did have fields across both environments were not spatially correlated (spatial correlation familiar to novel: 0.15+/-0.05). A new population of cells and fields was recruited to encode the novel environment, indicative of global remapping[32,38-40] (Figure 5C).

Lastly, we recorded the firing patterns of the CA1 populations before during and after the looming stimulation (Figure 5D). In addition to imaging during the first looming session (as described in Figure 4), we also applied a single looming stimulus on several subsequent sessions and imaged during these sessions as well (total of 11 looming sessions across 4 imaged mice, 2-3 sessions/mouse). As on the first looming session, mice displayed dramatic freezing and fleeing on subsequent days (immediate freezing in 4 of 11 sessions, fleeing followed by freezing in 7 of 11 sessions, mean freezing time to first movement 3.6+/-3.8 min; running speed of 22.9+/-8.7 cm/s in the minute before loom vs 9.8+/-4.9 cm/s in the minute after freezing, paired t-test, p=0.0016; including all time periods, average running speed after loom was 79% of speed before loom), with sustained CA1 activity for several seconds after the loom (Figure S5J). Interestingly, we found that many place cells with place fields in the middle of the track (around the loom location) before looming stimulation either lost their place fields or had their place fields move to a new track location in the trials after freezing. In contrast, place cells with place fields at the beginning and end of the track (first and last 50 cm of track) displayed less change in their place firing patterns (0.54 vs 0.67 spatial correlation values middle vs ends of track for before vs after looming; paired t-test, p=0.039). This difference was also seen using Bayesian decoding analysis (Figure 5E). The encoding model was built from (a subset of) trials before the looming stimulus and then used to decode mouse position either in (the remaining) trials before the stimulus or in the trials after the stimulus. While the decoding error before the looming stimulus was relatively low (23.6+/-12.7 cm), the error was significantly larger for trials after freezing (45.9+/-23.9 cm, p=0.02, paired t-test), with particularly larger decoding error in the middle compared to the ends of the track (53.3+/-24.9 cm vs 26.5+/-23.1 cm, p=0.0003, paired t-test). Interestingly, when we decoded mouse position during the freezing period, we found in several cases that the decoded position was persistently remote from the mouse's actual position (Figure 5F). For example, in one mouse that froze near the exit of the tunnel near the beginning of the track, the decoded position was further down the track at the location of the loom that had just occurred (mean of 112.3 cm away). In a different mouse, which froze in the open field, the decoded position was at the end of the track in the tunnel (mean of 79.8 cm away).

Discussion

Here, we developed VR goggles for mice in a system we refer to as iMRSIV. We show that mice engaged (performed anticipatory licking) more quickly in a virtual linear track task in the iMRSIV system compared to a

conventional monitor-based VR system. We hypothesize that this is because their full FOV was illuminated and the conflicting lab frame was not visible. This advantage, combined with the potential depth information provided by the stereoscopic illumination of the binocular region, may provide a more immersive experience, facilitating increased task engagement and spatial awareness. Alternatively, minor differences in screen brightness or the additional handling time needed at the start of iMRSIV sessions to align the system may play a role; further work will be needed to isolate the exact benefits of the iMRSIV system. By combining the iMRSIV system with functional two-photon microscopy, we established the existence of large populations of place cells during virtual linear track navigation and global remapping during a track change paradigm, all of which were highly similar to place cell recordings from previous VR and real-world experiments[12,32,41-44]. For a familiar linear track, properties of CA1 place cells were highly similar between our iMRSIV and 5-monitor cohorts (Figure S5), perhaps reflecting the capacity of the hippocampus to encode space across a wide range of contexts to produce stable internal maps.

Previous research has found different behavioral responses to side or front looming stimuli compared to overhead looming stimuli[36], emphasizing the importance of being able to access and visually stimulate the overhead region. We took advantage of the ability of the iMRSIV system to illuminate this region—a region difficult to illuminate with current VR systems. Similar to real-world looming stimulus paradigms[23,36,37], mice in iMRSIV displayed dramatic and long lasting freezing reactions, either immediately or after a short fleeing response. We were also able to provide the first descriptions of the response of place cell ensembles to overhead looming stimulation. We found that place fields around the looming location became unstable and significantly changed their firing patterns, while place fields farther away were more stable. Further, we found several examples during the freezing period itself where the decoded position differed significantly and persistently from the actual mouse location. The decoded position in these examples was either in the tunnel or around the loom location. Perhaps the mouse was thinking of a remote, safe location rather than the current, open field actual location, for planning purposes. Or perhaps the mouse was rehashing the location of the loom that had just occurred for memory consolidation. Future work will be required to establish the details and behavioral roles of these phenomena. While it might be possible to perform hippocampal recordings from freely moving mice with head-mounted microscopes or electrodes during overhead looming stimulation, there could be complications due to the head-mounted recording components[41,45-47] partially occluding the overhead binocular region (Figure 1C). iMRSIV does not suffer from these issues because the real-world overhead region is not seen by the mice.

An advantage of our iMRSIV system is the significant size reduction compared to existing rodent VR systems (~10x smaller). This miniaturization allows for the iMRSIV system to be more easily combined with a microscope or other recording systems that require significant space or are of an unusual geometry, and thus are not compatible with larger current VR systems. Further, the smaller footprint of iMRSIV is likely to facilitate the building and use of large scale training arrays where dozens of mice can be trained in parallel[26,27].

The following future experiments may be enabled by iMRSIV: 1) use of stereo depth for studies of object localization and predation[20,48]; 2) elimination of static lab frame visual inputs allowing for studies of visual flow, which may drive head direction signals in head-fixed mice[49]; 3) looming paradigms[23]; 4) improved depth perception may result in avoidance of perceived virtual cliffs, allowing for elevated maze tasks and measures of anxiety in VR. As more improvements to the immersiveness of VR are made, the gap between VR and freely moving experiments may continue to close. In parallel, technological improvements are enabling new studies such as multi-photon imaging in freely moving mice[46,50] or rotational head-fixed systems to add vestibular inputs to VR[51,52]. Each approach carries distinct advantages. VR offers the ability to dissect neural circuitry underlying behaviors using recording techniques that require physically large platforms that have yet to be miniaturized for use in freely moving rodents. Further, VR allows for manipulations that are impractical or impossible in physical environments. On the other hand, neural circuitry evolved to drive behavior in the freely moving case, and replicating the natural profiles of every sensory modality from freely moving rodents is a technically difficult endeavor for VR.

A limitation of our current iMRSIV system compared to conventional VR is the difficulty in tracking eye position and pupil size[53,54]. These measurements are relatively easy in a conventional system, but in the iMRSIV system there is little or no space for camera access. Thus, even though we provided a full 140-degree FOV with +/-20 degrees for saccades in each eye, we were not able to determine how much of this extra FOV the mice used

and how often they performed saccades. Thus, it will be important for future versions of the iMRSIV system to incorporate eye monitoring capabilities.

Due to steric hindrances between the iMRSIV display screens and the microscope objective, not all brain regions can be readily accessed (e.g. far rostral or lateral; Figure S5E-F). Further, some microscope objectives will have more severe steric hindrances. These issues may be physically impossible to avoid due to the large view angles of the mouse eye and its proximity to rostral and lateral brain regions. Indeed, most microscope objectives are probably within the mouse's visual fields when imaging rostral and lateral brain regions in a conventional setup. Long working distance objectives (as used here, along with its outer casing removed), thin GRIN lenses or tilting the head could be used for additional clearance. Also, Neuropixels are compatible with iMRSIV and could provide access to more brain regions (but with accommodations needed for the ~6x7x2mm headstage). In future versions, the iMRSIV system could be reduced in physical size by using a different lens design combined with a smaller screen, which would make it easier to access rostral and lateral brain region.

Another limitation of our system is the contact between the screens and mouse facial vibrissae (whiskers). This limits access to experimenters studying the whisker system and may reduce immersiveness of the system. While whisker trimming or future reductions in the size of iMRSIV may help, these are important limitations to consider when planning iMRSIV experiments.

Future improvements to the iMRSIV system could further increase immersiveness, such as higher resolution screens to further exceed mouse visual acuity or incorporating other sensory modalities such as olfactory[33], auditory[55,56] and tactile[57]. Further, here we used a cylindrical treadmill and linear track tasks, but 2D open field tasks are possible in head-fixed mice using the iMRSIV system with a spherical treadmill[1]. Though vestibular cues will be missing in rigid head-fixed systems, which might preclude proper activation of 2D spatial firing patters in place and grid cells, the iMRSIV system should be compatible with VR approaches that rotate the animal in conjunction with movements through the virtual space to activate the vestibular system[51,52]. Such a combination of techniques might lead to methods to study 2D navigation neural circuitry in head-fixed mice[58,59]. Finally, with future miniaturization, goggles small and light enough to be carried by a freely moving mouse might be achievable. Such a system could be used for augmented visual reality paradigms in which the other senses, including self-motion cues, are preserved.

Acknowledgments

We thank members of the Dombeck lab for comments on the manuscript. This work was supported by the National Institute of Health (R01-MH101297 to DAD), the National Science Foundation (NSF/ECCS-1835389 to DAD), the Hartwell Foundation (to JBI) and the Brain and Behavior Research Foundation (to JBI).

Author Contributions

DP, GD and DAD developed the iMRSIV concept. JBI, DP, GAD and DAD designed and built the system. DP, GD, JBI and GAD programmed the software. JBI, DP and DAD conceived and designed the experiments, analyzed the data, interpreted the data, and wrote the paper. DAD supervised all aspects of the project.

Declaration of Interests

D. Pinke and G. Dobos are on a patent related to this work: "Virtual reality simulator and method for small experimental animals" HU1900400A1.

Inclusion and Diversity

We support inclusive, diverse, and equitable conduct of research.

Main Figures

Figure 1: ***The mouse visual system and proposed concept for mouse VR goggles***

A. Mouse FOV with monocular (green) and binocular (red) regions shown at resting eye gaze position from top-down and front perspectives.
B. Simulated mouse in a cue rich environment, including overhead owl (left), with simulated 140-degree FOV from the two eyes (right). Note the different perspective from each eye of the cheese and owl objects in the binocular overlap region (highlighted in red).
C. Simulation of mouse FOV in a computer monitor based VR system (left), with simulated 140-degree FOV from the two eyes (right), binocular overlap region highlighted in red, and representation of overhead microscope (black rectangle above mouse). Note the large (black) region of the visual FOV that is not illuminated by the VR screens, no owl present since the overhead region is not rendered on the screens, and the same perspective from each eye of the cheese in the binocular region.
D. Simulation of the mouse FOV using the concept presented here using goggles (left), with simulated 140-degree FOV from the two eyes (right), and binocular overlap region highlighted in red. Note the different perspective from each eye of the cheese and owl objects in this region. Further, the full visual FOV is illuminated in each eye and the overhead microscope from **C** is not visible to the mouse in this setup. See also Figure S1.

***Figure 2:* iMRSIV goggle device design and validation**
A-E. Design and validation of Zemax simulation and mouse eye experiment for traditional monitor setup.
A. Zemax simulated mouse eye retina at a distance of 200mm from the checkerboard in B. Rays for 3 different object points are shown.
B. Checkerboard pattern used as the object in Zemax simulations.
C. Real-world reproduction of simulated arrangement, from side and top views. 482x261mm checkerboard shown on computer monitor 200 mm from an extracted mouse eye. Camera is used to view the back of the retina.
D. Resulting image of the checkerboard object on the Zemax simulated eye retina, view from the back of the retina.
E. Image of computer monitor checkerboard object on the retina of an extracted mouse eye, as viewed with the camera.
F-O. Design and validation of Zemax simulation and mouse eye experiment for iMRSIV (lens + display) concept.
F. Our optical system to achieve a 180-degree FOV using a custom designed positive-meniscus lens and a small curved illumination display, shown with mouse eye at the optimal location.
G. Zemax simulation of rays from different screen points traveling through mouse eye to the retina; blue, center of optical axis; red and green, edges of 140-degree eye FOV imaged onto retina; pink and yellow, edges of 180-degree FOV not imaged onto retina, but illuminated on screen for additional FOV for eye saccades.
H. Same as I, but zoomed in on eye.
I. Recreation of the checkerboard arrangement from **B**, **C**, but in a virtual world using Unity3D. 180-degree FOV of this scene was generated using a single Unity3D camera and a custom fish-eye shader. 140-degree FOV highlighted in red. Schematic shows 140-degree FOV and full 180-degree FOV to accommodate 20-degree saccades.
J. Eye model (as in **H**) and simulated recreation of checkerboard using custom fish-eye shader (as in **I**) after 20-degree saccade (gaze rotation).
K. Real optical iMRSIV system composed of curved screen and custom lens, along with experimental setup shown underneath.
L. The 180-degree FOV from **I** was shown on the small, curved display in Zemax as the object, which was imaged onto the mouse eye retina through the positive-meniscus lens; the resulting image of the checkerboard object on the Zemax simulated eye retina is shown here (140-degree eye FOV). View is from the back of the retina.
M. Checkerboard scene from **I** was used to illuminate the real OLED screen; the resulting image (through the real positive-meniscus lens) on the retina of an extracted mouse eye is shown, as viewed from a camera at the back of the retina.
N-O. Same as **L**, **M**, but with eye rotated 20-degrees with respect to screen center (as in ray diagram in **J**, left) to simulate 20-degree saccade. See also Figures S2-3 and Videos S1-2.

***Figure 3:* iMRSIV behavior apparatus and device-eye alignment procedures**

A. Left, iMRSIV system connected to 3D micro-positioners with metal bars, incorporated into a head-fixed behavior apparatus with treadmill and reward delivery system. Right, photo of mouse in iMRSIV system.

B. Zoom view from **A** showing iMRSIV system and head-plate positions with respect to mouse.

C. Schematic of electronics connections for control and reading from iMRSIV system, treadmill and reward delivery systems.

D. Left, 3D printed frame used during surgery to position the head-plate at the same location with respect to the eyes across different mice. Middle, view of frame on mouse and aligned to eyes. Right, zoomed in view.

E. Left, 3D printed frame with pointed target used to position each half of the iMRSIV system with respect to each eye before each session. Middle, view of frame on mount and target aligned to mouse eye. Right, back view.

F. Left, separated iMRSIV system components. Middle, iMRSIV system aligned to correct location with respect to mouse eyes (only one side is shown for clarity). Right, back view. See also Figure S4 and Video S3.

***Figure 4:* iMRSIV spatial behaviors: linear track and looming stimulation**

A. Linear track used for behavior, with tunnels (brown) and reward (blue) locations shown.

B. Trials/min over training days (sessions) for the conventional 5-panel VR group (left) and the iMRSIV group (right). Light grey lines show data for individual mice. Thick line and shading represent mean+/-SEM across mice. Dashed line reproduces mean for 5-panel group.

C. Top, prelicking index over training days for the 5-panel VR group (left) and the iMRSIV group (right). Bottom, mean licking rate vs. position (reward position, blue) over all mice in each group for days 1, 2 and 3 of training. Note the anticipatory licking in the iMRSIV group on day 1 is not present in the 5-panel group. * $p < 0.05$ between groups on day 1 using 2-sample t-test.

D. Linear track used for looming behavior, with tunnels (brown), reward (blue) and looming stimulation (black discs) locations shown.

E. Top, three examples of behavioral responses to the looming stimulus (dashed line) showing no change in running velocity for a 5-panel group mouse (left) and rapid freezing for one (middle) and fleeing followed by freezing in the other (right) iMRSIV group mice. Bottom, plots of mean velocity vs. time at looming onset (dashed lines) over all mice in each group. Quantification of freeze durations for each mouse across groups also shown, parsed by time to first movement and time to first run. Note the long-lasting freezing in the iMRSIV group that is not present in the 5-panel group. * $p < 0.05$ between groups on day 1 using 2-sample t-test. See also Figure S5.

***Figure 5:* Two-photon calcium imaging during iMRSIV spatial behaviors**

A. iMRSIV+2P. Example two-photon imaging field of CA1 neurons labeled with jGCaMP8m and regions of interest (ROIs). Imaging during familiar linear track navigation using iMRSIV.

B. Left, recording of 253 place cells in a single field. $\Delta F/F0$ vs. time for each neuron over several trials along with track position, running velocity and licking. Right, mean transient rate vs. track position for all place cells from 4 familiar environment sessions (n=4 mice; cross-validated even-odd laps) and histogram of place field peak locations.

C. Mean transient rate vs. track position for all place cells with fields in both environments during environment switch sessions (n=4 mice). Left, place fields in familiar track (cross-validated), scatter plot of place field peak locations (familiar even laps vs familiar odd laps), and histogram of place field peak locations; middle, place fields in novel track (cross-validated), scatter plot of place field peak locations (familiar laps vs novel laps), and spatial correlations between place fields—familiar odd vs familiar even, familiar vs novel, and novel odd vs novel even; right, place fields in novel track (cross-validated), scatter plot of place field peak locations (novel even laps vs novel odd laps), and histogram of place field peak locations. * $p < 0.05$ using 1-sample t-test.

D. Mean transient rate vs. track position for all place cells during looming sessions (n=4 mice, 11 imaging sessions). Left, place fields from pre-loom trials (cross-validated), scatter plot of place field peak locations (pre-loom even laps vs pre-loom odd laps); middle, place fields from post-loom trials, sorted based on pre-loom peak track locations, scatter plot of place field peak locations (pre-loom laps vs post-loom laps); right, place fields from post-loom trials (cross-validated), scatter plot of place field peak locations (post-loom even laps vs post-loom odd

laps); bottom, spatial correlations between place fields—pre-loom odd vs pre-loom even, pre-loom vs post-loom, and post-loom odd vs post-loom even, along with spatial correlations vs track position for the three comparisons. * $p < 0.05$ using 1-sample t-test.

E. Bayesian decoding of mouse location based on CA1 firing patterns. Top, example session showing actual mouse track location vs decoded position; encoding model built with some pre-loom trials and decoding applied to remaining pre-loom trials (left) or applied to post-loom trials (right). Bottom, decoding position error vs track position for pre-encoding/pre-decoding (left) and pre-encoding/post-decoding (right)—pre-pre reproduced in grey for comparison.

F. Two examples of decoded position probability vs time (heat maps, top) during several pre-loom trials and during the freezing periods, along with plots (bottom) of actual position (black) and decoded position (peak probability, orange). Note high correspondence between actual and decoded positions during pre-loom trials, but large difference between actual and decoded positions during the freezing periods. See also Figure S5.

STAR Methods

Key resources table

REAGENT or RESOURCE	SOURCE	IDENTIFIER
Bacterial and virus strains		
AAV9-syn-jGCaMP8m-WPRE	Addgene	RRID:Addgene_162375
Deposited data		
Processed behavior and 2p imaging data	This paper	10.5281/zenodo.8393062
Experimental models: Organisms/strains		
C57BL/6J	The Jackson Laboratory	RRID:IMSR_JAX:000664
BALB/C	Charles River	RRID:IMSR_CRL:028
Software and algorithms		
Unity 2021.2.9f1	Unity Technologies	https://unity.com
MATLAB R2022b	MathWorks	https://www.mathworks.com
OpticStudio 23.1.1	Zemax, LLC	https://www.zemax.com
Blender 3.5	The Blender Foundation	https://www.blender.org
Custom Unity scripts and VR environments	This paper	github.com/DombeckLab/IMRSIV and 10.5281/zenodo.10127394
Other		
Lens design in Zemax	This paper	github.com/DombeckLab/IMRSIV
STL files for custom-printed parts	This paper	github.com/DombeckLab/IMRSIV

Resource availability

Lead contact

Further information may be requested from and will be provided by the corresponding author, Daniel A. Dombeck (d-dombeck@northwestern.edu).

Materials availability

This study did not generate new unique reagents.

Data and code availability

- Lens design (in Zemax), 3D models of custom equipment used, and VR environments (in Unity) are available at an online repository (https://github.com/DombeckLab/IMRSIV). Data is available online as well (10.5281/zenodo.8393062).
- All original code has been deposited at 10.5281/zenodo.10127394 and is publicly available as of the date of publication. DOIs are listed in the key resources table.
- Any additional information required to reanalyze the data reported in this paper is available from the lead contact upon request.

Experimental model and study participant details

Animals

All animal procedures were approved by the Northwestern University Institutional Animal Care and Use Committee. Mice were housed in a vivarium with a reversed light/dark cycle (12 hours light during the night) and all experiments were performed during the day (during their dark cycle). For behavior and CA1 imaging experiments, ~12 week old adult C57BL/6J male mice (The Jackson Laboratory, strain #000664) were used. The use of only male mice for behavior is a potential limitation of this study. For extracted eye experiments, 10-14 week old adult BALB/c mice (Charles River) of both sexes were used. All mice were immunocompetent and were not used in any previous procedures and are thus otherwise naïve to any drug or test outside of the procedures described. Experiments were replicated using multiple cohorts of iMRSIV and control mice, with littermates randomly assigned to each group. Blinding was not possible, however, since it was clear to the experimenter which apparatus the mice were placed into. All mice implanted with headplates were included in analysis. No statistical methods were used to predetermine sample size. Sample sizes were calculated based on similar previously published studies.

Method details

Headplate and CA1 cannulation surgery

Headplates were aligned and attached to adult C57BL/6J male mice as detailed below. For a subset of 9 mice (4 iMRSIV and 5 control) mice, CA1 cannulation and virus injection was also performed to allow for imaging.

Anesthetized mice (1-2% isoflurane in 0.5 L/min O_2) were head-fixed to a stereotaxic apparatus (Model 1900, David Kopf Instruments). The skull was leveled and aligned to bregma. We then positioned the eyes relative to the headplate holder by using a custom 3D-printed alignment tool (Figure 3D). This tool has two prongs that approximate the position of the center of each eyeball. Once centered, the tool was replaced with a custom titanium headplate (1 mm thick, eMachineShop). This headplate is the same size and shape as the alignment tool but without the centering prongs. Further details on our alignment procedures are provided below under "iMRSIV alignment procedure". Dental cement (Metabond, Parkell) was used to adhere the headplate to the skull. Mice were monitored closely for 24 hours and given 3-5 days to recover before water restriction and behavioral training were begun.

In mice used for CA1 imaging, before attaching the headplate we performed a small craniotomy (0.5 mm) and, using a beveled glass micropipette, injected ~60 nL of AAV1-syn-jGCaMP8m-WPRE[60] (Addgene catalog #162375, diluted ~8x from 2.5e13 GC/ml stock into phosphate buffered solution) into right CA1 (2.3 mm caudal, 1.8 mm lateral, 1.3 mm beneath dura). Then a stainless steel cannula with an attached 2.5 mm No. 1 coverslip (Potomac Photonics) was implanted over CA1[12].

Extracted eye experiment

To measure the image formed on the mouse retina, we used explanted eyes from BALB/c mice. We chose to use albino mice because the retinal epithelium is not pigmented and thus images formed on the retina using the visible spectrum can be observed by photographing the back of the explanted eye. We chose this particular strain

(BALB/c) because the size of the eye and the optical parameters are highly similar to the strain of mice used for our behavior and imaging experiments (C57BL/6J)[61].

Mice were deeply anesthetized with isoflurane (2% in 0.5 L/min O_2). The eye was then removed, the optic nerve transected, and any connective tissue cleared. The eye was then placed on a custom 3D printed mount that centered the eye relative to the rest of the setup. For the setup, a camera (Basler acA5472 with a 25 mm f/1.4 lens, HR978NCNH1198) was mounted behind the eye while the display (either large flat-panel display or the iMRSIV lens and miniature display) were mounted in front of the eye. Using rotation and translation stages, we could control the distance from the displays to the eye and we could adjust the rotation of the eye relative to the display. We could also lock in the camera so that it rotated with the eye, or we could rotate it independently of the eye. The desired image was displayed on the screen and the image formed on the retina as observed from behind the eye (caudal view) or from the side (lateral view) was photographed using the camera.

Zemax simulations and updated eye model

Replicating the real-world full stereo vision of mice in virtual reality is optically challenging for a number of reasons. First, the mouse eye has a large angle FOV that spans 140 degrees plus another +/-20 degrees for saccades[18-20]. Not only does this large angle occupy a large space, it also requires solutions that account for the Petzval field curvature. Second, the binocular region requires a solution that can deliver different perspectives of the same object to each eye (thus transmitting binocular disparity information). Because these views physically overlap, either the two eyes need to receive different images from the same position (such as is accomplished when viewing 3D televisions through polarized lenses) or the optical field needs to be separated so that the physical space illuminating the medial portions of each eye are different.

To aid our testing, we used Zemax software to simulate the optics of our design solution. We began with a published model of the mouse eye[6] and modified the exact coverage of the retina. On the basis of published eye parameters[31,62], we expanded the retinal periphery to cover the 140+ degrees FOV (with a 3 mm eye diameter). For simulating retinal projections in Zemax, we used Image Simulation, Geometric Bitmap Analysis and Geometric Image Analysis with 3 mm diameter retina parameter (300x300 pixel, 0.01 pixel size), Pupil size was 0.4 mm to 1.6 mm to simulate constricted and dilated pupils as well. We then validated our updated model by comparing the results obtained from our extracted eye experiments (detailed above) using a fixed display with a checkerboard pattern and compared them to the Zemax simulation using identical parameters and the same display image (Figure 2).

Next, we sought to identify a lens design that, when placed between a miniature display and the mouse eye, could accomplish our design goals. In particular, we wanted a solution that would project 180-degrees of the visual field while also physically occupying a small footprint so that the displays for each eye would not intersect. We began with off-the-shelf lenses but found that plano-convex or bi-convex lenses would not be adequate to cover the 180-degree range. Instead, a positive-meniscus lens was used such that, across the curvature of the eye, we could preserve an approximately fixed distance between the lens and the eye. The lens is a custom design (manufactured by Shanghai Optics) with the following specifications: diameter = 12 mm, center thickness = 4 mm, front radius curvature = 6 mm, back radius curvature = 10 mm, material: H-K9L glass. Further, the display itself (6.3 mm from the front surface of the lens) needed to have some curvature as well to reduce distortions introduced when the display-to-lens distance varies across different angles. We used a display radius of curvature of 60 mm along the azimuthal axis. As the physical constraints of the display only allow for curvature along one axis, the display remained flat (not curved) along the other (vertical) axis. The difference in curvature did not introduce any substantially different distortions along the two axes (Figure S3B-E). Finally, the curved screens were both rotated 25-degrees, around the eye axis, vertically from the nose.

Once we had identified the exact parameters for the desired lens design in Zemax, we had the lens fabricated (Shanghai Optics). The actual lens and our design was then validated using the explanted eye as detailed above

and as shown in Figure 2. Custom 3D parts to mount the lens and display were printed using tough PLA on a 3D printer (UltiMaker S3).

Quantification of similarity between retina images

To compare a pair of retina images, our procedure involved choosing the individual vertices of the checkerboard pattern in both images. Then we calculated the Cartesian distance between each pair of vertices. This distance was then normalized by the size of the retina (3 mm). These distances were then averaged over columns or rows of the checkerboard to attain deviation distance as a function of the x-axis or y-axis, respectively.

We compared the Zemax image of the checkerboard for the monitor with the Zemax image of the same scene using iMRSIV. We found that the % deviation was small and much of the discrepancy was due to a difference in magnification between the images. The images were practically identical when the iMRSIV retina image is scaled up by 5% (Figure S2A-E).

Next, we compared the real mouse retina images to the various Zemax models (monitor, iMRSIV with the default configuration, and iMRSIV or monitor with a 20-degree rotation). Here, we first registered the images (rotation, translation, and scaling) and then calculated the % deviation. This was performed for several different experiments (different eyes from two mice), allowing us to estimate the standard deviation of this measure (Figure S2F-Q).

Unity environment and hardware

Virtual reality environments were rendered in Unity3D (see also: https://github.com/axolotlWorks/Moculus). The same computer was also used to synchronize behavior and two-photon imaging data during execution of VR simulations.

In the Unity environment, a model mouse was used to approximate the position and orientation of the mouse eyes. The angles were then replicated in the positions and orientations of the physical displays relative to the actual mouse (22-degrees vertical elevation from the lambda-bregma plane and 64-degrees azimuth from the midline).[8] We also needed to correct for the distortions of our custom lens. To accomplish this goal, we used a fisheye shader. Each eye's display is covered by a shader. A 360-degree sphere camera in Unity is projected by seven 90-degree cameras onto a sphere overlay. The sphere is captured by an 8th perspective (70-degree FOV) camera which was placed at 267 mm from the sphere. This fisheye projection corresponds to ~180 degrees FOV, projected onto one circular display. Our custom lens also provides a strong anti-fisheye effect (see https://www.mathworks.com/help/vision/ug/camera-calibration.html); we compared the fish-eye vs. anti-fisheye effect, and we found that they are approximately the opposite effect (inverse transforms), so there was no need to further correct the lens distortion (Figure S3A).

Each lens was then paired with a small, flexible, round OLED screen (1.39 in diameter, 400x400 pixel, Innolux).

For our control experiments using a traditional 5-monitor display, we used five cameras in Unity, angled at increments of 45º, to reproduce the physical locations of the monitors arranged as five sides of an octagon around the mouse. Each monitor was run at a resolution of 1920x1080[21].

Refresh rate for both systems (iMRSIV and 5 panel) was 60 Hz, which were driven by a video card (Nvidia RT3070). Monitor brightness per unit area was higher for the round OLED screens of iMRSIV than for the large monitors we used for the traditional 5-panel display. This brightness was measured by collecting light over a 5-mm diameter region of the display using a fiber optic cable pressed against the screen and light collected on the other side using a photodetector (DET-100A, Thorlabs). For a given uniform display (either 50% gray or 100% white), the voltage measured from the photodetector was ~10 fold higher for the OLED screens. However, the exact amount of light reaching the mouse retina in each system is difficult to approximate exactly and is further complicated by differences in pupil diameter (which was not measured here). Overall brightness is a function

involving integration of light from all portions of the screens, and an inverse square law describing the reduction in intensity as a function of distance from the source. Based on our estimates of these values, the overall brightness received by the mouse eye was higher in the iMRSIV system. Thus, for particular future applications, the intensity of the virtual environments could be reduced as needed.

Custom scripts were written in C# to enable communication with a data acquisition card (PCIe-6323, National Instruments) from within the Unity runtime environment. We took advantage of the fixed update clock (set to 1 ms) within Unity to gain precise control of all timed events. The data acquisition card (DAQ) was used to output timed digital output to control the opening of a water reward solenoid. The timing was calibrated to provide a volume of 3 μL of water. Inputs to the DAQ included a quadrature encoder and digital signals. The quadrature encoder was used to read running velocity from an optical encoder (E2-5000, US Digital) attached to the axis of the treadmill. These values were converted to a calibrated position along the treadmill in centimeters, which was then used to move the position of the mouse in Unity. Digital inputs were used to read contact between the tongue and the lick spout using a capacitive touch sensor (AT42QT1010, SparkFun) and also two-photon frame times. These signals were all read by the DAQ at 1 kHz. All DAQ data along with environmental variables from Unity (such as mouse position in the VR world, velocity, etc.) were continuously stored during each frame in a dat file. Thus, we could precisely synchronize environmental variables with two-photon imaging frames when processing the data. A 3-axis translation stage was used to position the lickport (DT12XYZ, Thorlabs).

iMRSIV alignment procedure

To position the iMSRIV displays relative to each mouse eye, we developed the following alignment procedure that minimized mouse-to-mouse variability while also permitting adjustments to be made for each mouse. We utilized a custom-designed headplate with a couple features that facilitated our experimental approach. First, the grooves for mounting to the headbars were positioned further posteriorly, thus adding clearance from the head mounting bars for the iMRSIV lens + display (and also remaining outside the field-of-view of each eye). Second, the grooves were positioned exactly 30 mm apart, thus allowing precise and reliable mounting using off-the-shelf parts (such as the Thorlabs 30 mm cage system). During surgical implantation, the headbar is aligned to the eyes of each mouse. This alignment is accomplished by first using a custom 3D-printed alignment tool (Figure 3D). This tool has two prongs situated for positioning to the center of each eyeball. Once the tool is aligned (prongs centered on each eye), the stereotax micromanipulator is fixed while the tool is replaced with a headplate and cemented in place. Thus, the relative position of the headplate mount to the eyes of the individual mouse is fixed (within experimental measurement error).

We also measured the position of the eyes with respect to bregma and found some variability in the position of the eyes relative to bregma. For example, across a cohort of 7 mice, our standard deviation in bregma-eye distance is 0.11 mm medial-lateral, 0.34 mm anterior-posterior, and 0.21 mm dorsal-ventral. However, because we align to the eyes themselves, this variability does not affect our alignment and only slightly affects the accessible brain regions (Figure S5D-F). Note also that we placed the headplate with the skull leveled to 0 degrees (zero tilt between bregma and lambda), but it is possible that the headplate could be angled without perturbing the visual experience of the mouse.

During behavioral sessions, the headplate is attached to the headbars. To verify the placement of the mouse and that the eyes are correctly positioned relative to the iMRSIV displays, we utilized the following alignment procedure. The goal was to position the display assembly (consisting of the lens-holder attached to the display holder) at the desired position relative to the mouse eye lens (Figure 2F,G, Figure 3). The lens-holder and display holder are attached using a set of 3 magnets, allowing us to attach and detach the lens-holder in a reproducible manner. The assembly is attached to a 3-axis stage (3x MS1S, Thorlabs), allowing precise control of x-y-z position, along with a rotation stage (RP005, Thorlabs). To perform the alignment, first an alignment tool (Figure 3E) was attached in place of the lens-holder. This tool is similar to the lens-holder but instead of the lens has a probe at the desired location of the center of the front of the mouse eye lens. Thus, we could position the probe at

the eye lens, retract the assembly using the micromanipulator, replace the alignment tool with the lens-holder, and return the assembly back to the same position. Any final fine adjustments are then performed using micromanipulators for each iMRSIV display. In practice, however, we found that little to no adjustments were needed between mice.

To measure the precision of our alignment procedures, we replicated our alignment procedure using a replica eye (3.1 mm diameter ball bearing) placed on an xyz translation stage with micrometers precise to <25 microns (PT3, Thorlabs). Briefly, we aligned our target to the center of the ball bearing (Figure 3E), replaced the target with the iMRSIV lens, and then measured how far the center of the ball bearing was from the center of the lens by using the translation stage to align the ball bearing to the center of the lens (confirmed with a video camera, as in Figure 2C). We then read off the micropositioner distances needed to center the ball bearing. We repeated this procedure 5 separate times and found x,y errors were 0.31+/-0.14 mm and 0.16+/-0.05 mm. Meanwhile, our z-distance, which measured the distance between the front edge of the bearing to the iMRSIV lens surface, was 1.10+/-0.10 mm, which is within range of the desired 1.0 mm eye-lens distance. We simulated the effect of various misalignments using Zemax and the results, as shown in Figure S4, indicate that minimal image distortions are incurred (typically less than the visual acuity of mice) for the positioning errors expected during actual experiments.

Behavior

Following recovery from surgery, mice were restricted to receiving 0.8-1.0 mL of water each day. Mice were weighed daily and training was begun once weights fell to ~80% of baseline.

For iMRSIV mice, once the mouse was head-fixed, an alignment procedure was performed as detailed above ("iMRSIV alignment procedure") and in Figure 3. Note that it was not possible to perform truly blinded experiments when comparing iMRSIV mice to the 5-monitor control mice. We however matched training conditions in every aspect that we could by using mice of the same age, water restricting for the same duration with the same target weight, matching the duration of training sessions, etc. We also practiced the iMRSIV alignment procedures beforehand so as to minimize the time and potential discomfort incurred while positioning the screens around the mouse. Once proficient, we were able to perform this alignment within a couple minutes.

Once aligned, the training session was begun. Virtual environments were simulated in Unity. All environments consisted of the same basic structure. Mice start in a tunnel, run to reach a fixed reward location where a water reward is delivered to the lick spout, then continue running to the end of the track, which consists of a tunnel as well. The mice then teleport back to the start tunnel and the task repeats. Track lengths are 3 to 3.5 m. The first stage of training consisted of six sessions, one per day, each lasting ~40 minutes. These were performed in the first linear track. On the next day, a remapping experiment was performed. After at least 10 minutes in the familiar environment (typically 30-40 laps or more), mice were instantly teleported to a novel environment[32].

Looming stimuli were then presented in the next two or three sessions. For these experiments, a single loom event was simulated in Unity. The loom consisted of an overhead black disk[23], which also cast a dark shadow on the ground. The loom sphere (d=37.8 mm) was placed at a height of 200 mm from the mouse, with no visibility initially. After 10 minutes, whenever the mouse next entered into the trigger zone, the loom event was activated. The sphere became visible and started following the mouse without initially descending. As soon as it caught up, the loom sequence began. It descended from 200 mm to a height of 11 mm in 0.3 seconds, remained close for 0.25 seconds, and then returned to 200 mm. The loom descent repeated 3 times, following the animal's position. Thus, the exact position at which the looming stimulus occurred varied slightly depending on the animal's exact running behavior. The loom parameters (size, speed, position, and number of repeats) are parameters that can be changed within Unity.

Imaging

In the subset of cannulated mice, we performed two-photon imaging of populations of neurons in CA1 of the hippocampus during behavior sessions as described above, either with iMRSIV (4 mice) or with the traditional 5-panel display (5 mice). Imaging was performed using a customized upright microscope. A mode-locked Ti:Sapphire laser (Chameleon Ultra II, Coherent) tuned to 920 nm was raster scanned using a resonant scanning module (Sutter Instruments). Emission light was filtered (FF01-510/84, Semrock) before being collected by a GaAsP PMT (H10770PA-40, Hamamatsu Photonics). ScanImage software (Vidrio) was used to control the microscope and acquire images. A TTL frame sync signal was output to the DAQ of the VR computer to allow for synchronization of two-photon imaging times to the behavior data acquired by Unity. All imaging was performed at 512x512 pixels and 30 Hz using bidirectional scanning.

A 10X objective (UPLFLN, Olympus), with outer housing removed to fit within the geometric constraints, was used for imaging. We removed the outer housing of the objective (unscrewing it) to increase clearance between the objective and the iMRSIV lens-holder. In Figure S5D-F, we delineate regions of the cortex that are accessible using this objective without physically colliding with the iMRSIV lens mounts. As the placement of our headplate (and the iMRSIV system) is relative to the eyes of the animal, the exact relative location of bregma can vary across mice (and correspondingly the position of brain structures relative to bregma will vary as well). For example, across a cohort of 7 mice, our standard deviation in bregma-eye distance is 0.11 mm medial-lateral, 0.34 mm anterior-posterior, and 0.21 mm dorsal-ventral; thus, there is an uncertainty of ~0.25 mm in the boundary of which cortical regions would be accessible with the 10X objective (with removed housing) as shown in Figure S5D-F. Note that, in a traditional virtual reality system, the objective is within the overhead FOV of the mouse's vision (Figure 1C). To prevent iMRSIV display light from reaching the optical path and contaminating the emission PMT, we designed a custom shielding system that consisted of a 3D printed part that fit around the objective and connected to a ring on the head of the mouse. All data was collected at a magnification of 2.0X, which resulted in a field-of-view of 450 μm x 450 μm.

Image processing

Two-photon movies were first registered to correct for motion artifacts using rigid registration[63]. Next, active cells were detected using Suite2p. Fluorescence traces (brightness-over-time signals) for these cells and associated neuropil were extracted. Then, we used an integrated iterative algorithm to decompose the signal into an inferred summation of four signals: the true activity of the cell ($\Delta F/F_0$), the baseline (F_0), the neuropil contamination, and noise. We assume $\Delta F/F_0$ is the result of convolution of voltage action potentials with a kernel that reflects the kinetics of intracellular Ca^{2+} and the Ca^{2+} sensor jGCaMP8m. Thus, deconvolution is performed to infer firing events[64]. For further analysis, we use these firing events after smoothing with a 170-ms Gaussian filter. The "transient rate" refers to the amplitude and frequency of these detected events in a given time window or spatial bin.

Analysis

Prelicking index: This measure quantified whether mice were licking near to the reward during reward approach, indicative of learning of the reward location and anticipation of the reward. We took lick1 as the mean number of licks over the 50 cm leading up to the reward location (pre-reward zone: -50 to 0 cm relative to reward location) and lick2 as the mean number of licks in the preceding 150 cm (-200 to -50 cm relative to reward location). The prelicking ratio was then calculated as lick1/(lick1+lick2). Thus, the minimum possible value of 0 indicates no licks in the pre-reward zone while the maximum possible value of 1 indicates all the licks were in the pre-reward zone. We excluded laps if no licks occurred in the defined windows (both lick1 and lick2 equal to zero). In rare cases, the lick sensor did not function properly and registered contact throughout. Such laps were detected when the mean contact time across an entire lap was over 40% and were also excluded.

Loom reaction: We qualitatively assessed the initial reaction of mice to the looming stimulus by looking at the running velocity in the 10 seconds around the loom initiation time. Freeze: running velocity immediately decreases and is held at 0 cm/s for an extended period (often for minutes). Flee: running velocity immediately

increases, followed after a few seconds by an extended period of freezing. No reaction: no change in velocity from the prior moments and no extended period of stationarity.

Loom freezing period: For mice that did freeze, we measured the time when mice resumed running. Such running was found by looking for the first moment the running velocity reached half of the maximum running velocity, which was calculated for each mouse as the 98th percentile of running velocity over the entire session. We ignored the first 10 seconds immediately after the loom since some mice initially and transiently increased their running velocity (fleeing) before freezing. We also measured the freezing time until first detected movement since it was possible the mouse resumed movement but without running. To ensure that the treadmill velocity faithfully reported any movements (and not just running), we recorded video of the mouse's body during the loom sessions. We quantified the energy in a region-of-interest around the body of the mouse (mean across pixels of the square of the time derivative of individual pixels in the region) and found a high correspondence to the treadmill velocity (Figure S5A-C).

Criteria for place cells: For each neuron, spatial information was calculated using binned position (5 mm bins, periods of immobility and reward consumption excluded)[65]. The calculation was repeated using shuffled data. Neurons with spatial information of at least 0.75 bits/event and that was also larger than 98% or more of shuffles were categorized as place cells.

Calculation of peak location: For each place cell, mean transient rate at each position (1 cm bins) was calculated across laps. The peak location was calculated as the position with the maximal mean transient rate.

Reliability score: For each place cells, we calculated the fraction of laps at which significant firing occurred within the dominant place field of that neuron[12].

Cross-validation procedure: Spatial firing maps and other within-environment calculations used cross-validated data. In these cases, data was separated by even and odd laps.

Calculation of correlations: At each position, the Pearson correlation was measured between the vector of population firing under two conditions, thus quantifying similarity of individual neural firing. The two conditions were either taken as the comparison of odd and even laps (for example, with familiar-familiar measures) or all laps across conditions (for example, for familiar-novel measures). The values were then averaged across all positions. For comparison of correlations across positions, we compared the mean correlations on the ends of the track (first and last 50 cm) against the mean correlations in the middle of the track (entire track excluding the first and last 50 cm).

Bayesian decoding: For a given imaging session, population neural activity was used to decode the position of the track. This procedure was performed in two ways. First, for assessing the ability of pre-loom activity to decode post-loom position, we trained the Bayesian decoder[66] using the pre-loom data after binning the data using position along the track. This information was then used to decode the post-loom data, again after already binning for position along the track. For comparison, we also decoded pre-loom position using pre-loom data by splitting the data into odd laps (training set) and even laps (test set). Second, we assessed the decoded position during the freezing period in response to the loom stimulus. To perform this calculation, we trained the Bayesian decoder using all the pre-loom data. This decoder was then applied to the neural activity during the time that the mouse froze in response to the loom stimulus.

Quantification and statistical analysis

Statistical tests used in the paper are indicated where appropriate. Results are reported as mean+/-standard deviation unless otherwise indicated. MATLAB built-in functions were used to perform the statistical tests. The number of animals used is indicated in the figure or in the text, as appropriate. In some cases, we instead report

the number of imaging sessions ('FOVs'); in these cases, the figure legend indicates how many mice were used. Significance was set at $p < 0.05$. To determine whether data met assumptions for the statistical approach, the distribution of the data was visualized to decide between using parametric or non-parametric tests as indicated.

Supplemental Videos

Video S1. Image formed on real eye retina by iMRSIV checkerboard. Movie shows view of back of retina from different angles, related to Figure 2.

Video S2. Image formed on real eye retina by iMRSIV of 3D VR scene. Movie shows view of back of retina from different angles, related to Figure 2.

Video S3. 3-D model of head-fixed mouse in iMSRIV system with concurrent 2-photon imaging, related to Figure 3.

References

1. Dombeck, D.A., Khabbaz, A.N., Collman, F., Adelman, T.L., and Tank, D.W. (2007). Imaging large-scale neural activity with cellular resolution in awake, mobile mice. Neuron *56*, 43-57.
2. Sofroniew, N.J., Flickinger, D., King, J., and Svoboda, K. (2016). A large field of view two-photon mesoscope with subcellular resolution for in vivo imaging. Elife *5*. 10.7554/eLife.14472.
3. Stringer, C., Pachitariu, M., Steinmetz, N., Carandini, M., and Harris, K.D. (2019). High-dimensional geometry of population responses in visual cortex. Nature *571*, 361-365. 10.1038/s41586-019-1346-5.
4. Yu, C.H., Stirman, J.N., Yu, Y., Hira, R., and Smith, S.L. (2021). Diesel2p mesoscope with dual independent scan engines for flexible capture of dynamics in distributed neural circuitry. Nat Commun *12*, 6639. 10.1038/s41467-021-26736-4.
5. Petersen, C.C., Hahn, T.T., Mehta, M., Grinvald, A., and Sakmann, B. (2003). Interaction of sensory responses with spontaneous depolarization in layer 2/3 barrel cortex. Proc Natl Acad Sci U S A *100*, 13638-13643. 10.1073/pnas.2235811100.
6. Margrie, T.W., Brecht, M., and Sakmann, B. (2002). In vivo, low-resistance, whole-cell recordings from neurons in the anaesthetized and awake mammalian brain. Pflugers Arch *444*, 491-498. 10.1007/s00424-002-0831-z.
7. Yu, J., Gutnisky, D.A., Hires, S.A., and Svoboda, K. (2016). Layer 4 fast-spiking interneurons filter thalamocortical signals during active somatosensation. Nat Neurosci *19*, 1647-1657. 10.1038/nn.4412.
8. Smith, S.L., Smith, I.T., Branco, T., and Hausser, M. (2013). Dendritic spikes enhance stimulus selectivity in cortical neurons in vivo. Nature *503*, 115-120. 10.1038/nature12600.
9. Jia, X., Siegle, J.H., Durand, S., Heller, G., Ramirez, T.K., Koch, C., and Olsen, S.R. (2022). Multi-regional module-based signal transmission in mouse visual cortex. Neuron *110*, 1585-1598 e1589. 10.1016/j.neuron.2022.01.027.
10. Jun, J.J., Steinmetz, N.A., Siegle, J.H., Denman, D.J., Bauza, M., Barbarits, B., Lee, A.K., Anastassiou, C.A., Andrei, A., Aydin, C., et al. (2017). Fully integrated silicon probes for high-density recording of neural activity. Nature *551*, 232-236. 10.1038/nature24636.
11. Cohen, J.D., Bolstad, M., and Lee, A.K. (2017). Experience-dependent shaping of hippocampal CA1 intracellular activity in novel and familiar environments. Elife *6*. 10.7554/eLife.23040.
12. Dombeck, D.A., Harvey, C.D., Tian, L., Looger, L.L., and Tank, D.W. (2010). Functional imaging of hippocampal place cells at cellular resolution during virtual navigation. Nature neuroscience *13*, 1433-1440.
13. Harvey, C.D., Collman, F., Dombeck, D.A., and Tank, D.W. (2009). Intracellular dynamics of hippocampal place cells during virtual navigation. Nature *461*, 941-946. 10.1038/nature08499.

14. Campbell, M.G., Ocko, S.A., Mallory, C.S., Low, I.I.C., Ganguli, S., and Giocomo, L.M. (2018). Principles governing the integration of landmark and self-motion cues in entorhinal cortical codes for navigation. Nat Neurosci *21*, 1096-1106. 10.1038/s41593-018-0189-y.
15. Gauthier, J.L., and Tank, D.W. (2018). A Dedicated Population for Reward Coding in the Hippocampus. Neuron *99*, 179-193 e177. 10.1016/j.neuron.2018.06.008.
16. Harvey, C.D., Coen, P., and Tank, D.W. (2012). Choice-specific sequences in parietal cortex during a virtual-navigation decision task. Nature *484*, 62-68. 10.1038/nature10918.
17. Pinto, L., Rajan, K., DePasquale, B., Thiberge, S.Y., Tank, D.W., and Brody, C.D. (2019). Task-Dependent Changes in the Large-Scale Dynamics and Necessity of Cortical Regions. Neuron *104*, 810-824 e819. 10.1016/j.neuron.2019.08.025.
18. Scholl, B., Burge, J., and Priebe, N.J. (2013). Binocular integration and disparity selectivity in mouse primary visual cortex. J Neurophysiol *109*, 3013-3024. 10.1152/jn.01021.2012.
19. Boone, H.C., Samonds, J.M., Crouse, E.C., Barr, C., Priebe, N.J., and McGee, A.W. (2021). Natural binocular depth discrimination behavior in mice explained by visual cortical activity. Curr Biol *31*, 2191-2198 e2193. 10.1016/j.cub.2021.02.031.
20. Holmgren, C.D., Stahr, P., Wallace, D.J., Voit, K.M., Matheson, E.J., Sawinski, J., Bassetto, G., and Kerr, J.N. (2021). Visual pursuit behavior in mice maintains the pursued prey on the retinal region with least optic flow. Elife *10*. 10.7554/eLife.70838.
21. Heys, J.G., Rangarajan, K.V., and Dombeck, D.A. (2014). The functional micro-organization of grid cells revealed by cellular-resolution imaging. Neuron *84*, 1079-1090. 10.1016/j.neuron.2014.10.048.
22. Wallace, D.J., Greenberg, D.S., Sawinski, J., Rulla, S., Notaro, G., and Kerr, J.N. (2013). Rats maintain an overhead binocular field at the expense of constant fusion. Nature *498*, 65-69. 10.1038/nature12153.
23. Yilmaz, M., and Meister, M. (2013). Rapid innate defensive responses of mice to looming visual stimuli. Curr Biol *23*, 2011-2015. 10.1016/j.cub.2013.08.015.
24. Ravassard, P., Kees, A., Willers, B., Ho, D., Aharoni, D.A., Cushman, J., Aghajan, Z.M., and Mehta, M.R. (2013). Multisensory control of hippocampal spatiotemporal selectivity. Science (New York, N.Y.) *340*, 1342-1346. 10.1126/science.1232655.
25. Minderer, M., Harvey, C.D., Donato, F., and Moser, E.I. (2016). Neuroscience: Virtual reality explored. Nature *533*, 324-325. 10.1038/nature17899.
26. Bollu, T., Whitehead, S.C., Prasad, N., Walker, J., Shyamkumar, N., Subramaniam, R., Kardon, B., Cohen, I., and Goldberg, J.H. (2019). Automated home cage training of mice in a hold-still center-out reach task. J Neurophysiol *121*, 500-512. 10.1152/jn.00667.2018.
27. Poddar, R., Kawai, R., and Olveczky, B.P. (2013). A fully automated high-throughput training system for rodents. PLoS One *8*, e83171. 10.1371/journal.pone.0083171.
28. Ding, X.Q., Tan, J.Z., Meng, J., Shao, Y.L., Shen, M.X., and Dai, C.X. (2023). Time-Serial Evaluation of the Development and Treatment of Myopia in Mice Eyes Using OCT and ZEMAX. Diagnostics *13*. ARTN 379

10.3390/diagnostics13030379.
29. Gardner, M.R., Katta, N., Rahman, A.S., Rylander, H.G., and Milner, T.E. (2018). Design Considerations for Murine Retinal Imaging Using Scattering Angle Resolved Optical Coherence Tomography. Appl Sci-Basel *8*. ARTN 2159

10.3390/app8112159.
30. Wong, A.A., and Brown, R.E. (2006). Visual detection, pattern discrimination and visual acuity in 14 strains of mice. Genes Brain Behav *5*, 389-403. 10.1111/j.1601-183X.2005.00173.x.
31. Sterratt, D.C., Lyngholm, D., Willshaw, D.J., and Thompson, I.D. (2013). Standard anatomical and visual space for the mouse retina: computational reconstruction and transformation of flattened retinae with the Retistruct package. PLoS Comput Biol *9*, e1002921. 10.1371/journal.pcbi.1002921.
32. Sheffield, M.E.J., Adoff, M.D., and Dombeck, D.A. (2017). Increased Prevalence of Calcium Transients across the Dendritic Arbor during Place Field Formation. Neuron *96*, 490-504 e495. 10.1016/j.neuron.2017.09.029.
33. Radvansky, B.A., and Dombeck, D.A. (2018). An olfactory virtual reality system for mice. Nat Commun *9*, 839. 10.1038/s41467-018-03262-4.

34. Pettit, N.L., Yuan, X.C., and Harvey, C.D. (2022). Hippocampal place codes are gated by behavioral engagement. Nat Neurosci *25*, 561-566. 10.1038/s41593-022-01050-4.
35. Radvansky, B.A., Oh, J.Y., Climer, J.R., and Dombeck, D.A. (2021). Behavior determines the hippocampal spatial mapping of a multisensory environment. Cell Rep *36*, 109444. 10.1016/j.celrep.2021.109444.
36. Solomon, S.G., Janbon, H., Bimson, A., and Wheatcroft, T. (2023). Visual spatial location influences selection of instinctive behaviours in mouse. R Soc Open Sci *10*, 230034. 10.1098/rsos.230034.
37. Shang, C., Chen, Z., Liu, A., Li, Y., Zhang, J., Qu, B., Yan, F., Zhang, Y., Liu, W., Liu, Z., et al. (2018). Divergent midbrain circuits orchestrate escape and freezing responses to looming stimuli in mice. Nat Commun *9*, 1232. 10.1038/s41467-018-03580-7.
38. Muller, R.U., and Kubie, J.L. (1987). The effects of changes in the environment on the spatial firing of hippocampal complex-spike cells. J Neurosci *7*, 1951-1968. 10.1523/JNEUROSCI.07-07-01951.1987.
39. Leutgeb, S., Leutgeb, J.K., Barnes, C.A., Moser, E.I., McNaughton, B.L., and Moser, M.B. (2005). Independent codes for spatial and episodic memory in hippocampal neuronal ensembles. Science (New York, N.Y.) *309*, 619-623. 10.1126/science.1114037.
40. Dong, C., Madar, A.D., and Sheffield, M.E.J. (2021). Distinct place cell dynamics in CA1 and CA3 encode experience in new environments. Nat Commun *12*, 2977. 10.1038/s41467-021-23260-3.
41. Ziv, Y., Burns, L.D., Cocker, E.D., Hamel, E.O., Ghosh, K.K., Kitch, L.J., El Gamal, A., and Schnitzer, M.J. (2013). Long-term dynamics of CA1 hippocampal place codes. Nat Neurosci *16*, 264-266. 10.1038/nn.3329.
42. Kaufman, A.M., Geiller, T., and Losonczy, A. (2020). A Role for the Locus Coeruleus in Hippocampal CA1 Place Cell Reorganization during Spatial Reward Learning. Neuron *105*, 1018-1026 e1014. 10.1016/j.neuron.2019.12.029.
43. McNaughton, B.L., Barnes, C.A., and O'Keefe, J. (1983). The contributions of position, direction, and velocity to single unit activity in the hippocampus of freely-moving rats. Exp Brain Res *52*, 41-49. 10.1007/BF00237147.
44. Nakazawa, K., Sun, L.D., Quirk, M.C., Rondi-Reig, L., Wilson, M.A., and Tonegawa, S. (2003). Hippocampal CA3 NMDA receptors are crucial for memory acquisition of one-time experience. Neuron *38*, 305-315. 10.1016/s0896-6273(03)00165-x.
45. Juavinett, A.L., Bekheet, G., and Churchland, A.K. (2019). Chronically implanted Neuropixels probes enable high-yield recordings in freely moving mice. Elife *8*. 10.7554/eLife.47188.
46. Zong, W., Obenhaus, H.A., Skytoen, E.R., Eneqvist, H., de Jong, N.L., Vale, R., Jorge, M.R., Moser, M.B., and Moser, E.I. (2022). Large-scale two-photon calcium imaging in freely moving mice. Cell *185*, 1240-1256 e1230. 10.1016/j.cell.2022.02.017.
47. Voigts, J., Newman, J.P., Wilson, M.A., and Harnett, M.T. (2020). An easy-to-assemble, robust, and lightweight drive implant for chronic tetrode recordings in freely moving animals. J Neural Eng *17*, 026044. 10.1088/1741-2552/ab77f9.
48. Johnson, K.P., Fitzpatrick, M.J., Zhao, L., Wang, B., McCracken, S., Williams, P.R., and Kerschensteiner, D. (2021). Cell-type-specific binocular vision guides predation in mice. Neuron *109*, 1527-1539 e1524. 10.1016/j.neuron.2021.03.010.
49. Sit, K.K., and Goard, M.J. (2023). Coregistration of heading to visual cues in retrosplenial cortex. Nat Commun *14*, 1992. 10.1038/s41467-023-37704-5.
50. Klioutchnikov, A., Wallace, D.J., Sawinski, J., Voit, K.M., Groemping, Y., and Kerr, J.N.D. (2023). A three-photon head-mounted microscope for imaging all layers of visual cortex in freely moving mice. Nat Methods *20*, 610-616. 10.1038/s41592-022-01688-9.
51. Chen, G., King, J.A., Lu, Y., Cacucci, F., and Burgess, N. (2018). Spatial cell firing during virtual navigation of open arenas by head-restrained mice. Elife *7*. 10.7554/eLife.34789.
52. Voigts, J., and Harnett, M.T. (2020). Somatic and Dendritic Encoding of Spatial Variables in Retrosplenial Cortex Differs during 2D Navigation. Neuron *105*, 237-245 e234. 10.1016/j.neuron.2019.10.016.
53. McGinley, M.J., David, S.V., and McCormick, D.A. (2015). Cortical Membrane Potential Signature of Optimal States for Sensory Signal Detection. Neuron *87*, 179-192. 10.1016/j.neuron.2015.05.038.
54. Meyer, A.F., O'Keefe, J., and Poort, J. (2020). Two Distinct Types of Eye-Head Coupling in Freely Moving Mice. Curr Biol *30*, 2116-2130 e2116. 10.1016/j.cub.2020.04.042.

55. Runyan, C.A., Piasini, E., Panzeri, S., and Harvey, C.D. (2017). Distinct timescales of population coding across cortex. Nature *548*, 92-96. 10.1038/nature23020.
56. Gao, S., Webb, J., Mridha, Z., Banta, A., Kemere, C., and McGinley, M. (2020). Novel Virtual Reality System for Auditory Tasks in Head-fixed Mice. Annu Int Conf IEEE Eng Med Biol Soc *2020*, 2925-2928. 10.1109/EMBC44109.2020.9176536.
57. Sofroniew, N.J., Cohen, J.D., Lee, A.K., and Svoboda, K. (2014). Natural whisker-guided behavior by head-fixed mice in tactile virtual reality. J Neurosci *34*, 9537-9550. 10.1523/JNEUROSCI.0712-14.2014.
58. Hafting, T., Fyhn, M., Molden, S., Moser, M.B., and Moser, E.I. (2005). Microstructure of a spatial map in the entorhinal cortex. Nature *436*, 801-806. 10.1038/nature03721.
59. O'Keefe, J., and Dostrovsky, J. (1971). The hippocampus as a spatial map. Preliminary evidence from unit activity in the freely-moving rat. Brain research *34*, 171-175.
60. Zhang, Y., Rozsa, M., Liang, Y., Bushey, D., Wei, Z., Zheng, J., Reep, D., Broussard, G.J., Tsang, A., Tsegaye, G., et al. (2023). Fast and sensitive GCaMP calcium indicators for imaging neural populations. Nature *615*, 884-891. 10.1038/s41586-023-05828-9.
61. Puk, O., Dalke, C., Favor, J., de Angelis, M.H., and Graw, J. (2006). Variations of eye size parameters among different strains of mice. Mamm Genome *17*, 851-857. 10.1007/s00335-006-0019-5.
62. Zhang, P., Mocci, J., Wahl, D.J., Meleppat, R.K., Manna, S.K., Quintavalla, M., Muradore, R., Sarunic, M.V., Bonora, S., Pugh, E.N., Jr., and Zawadzki, R.J. (2018). Effect of a contact lens on mouse retinal in vivo imaging: Effective focal length changes and monochromatic aberrations. Exp Eye Res *172*, 86-93. 10.1016/j.exer.2018.03.027.
63. Guizar-Sicairos, M., Thurman, S.T., and Fienup, J.R. (2008). Efficient subpixel image registration algorithms. Opt Lett *33*, 156-158. 10.1364/ol.33.000156.
64. Friedrich, J., Zhou, P., and Paninski, L. (2017). Fast online deconvolution of calcium imaging data. PLoS Comput Biol *13*, e1005423. 10.1371/journal.pcbi.1005423.
65. Climer, J.R., and Dombeck, D.A. (2021). Information Theoretic Approaches to Deciphering the Neural Code with Functional Fluorescence Imaging. eNeuro *8*. 10.1523/ENEURO.0266-21.2021.
66. Etter, G., Manseau, F., and Williams, S. (2020). A Probabilistic Framework for Decoding Behavior From in vivo Calcium Imaging Data. Front Neural Circuits *14*, 19. 10.3389/fncir.2020.00019.

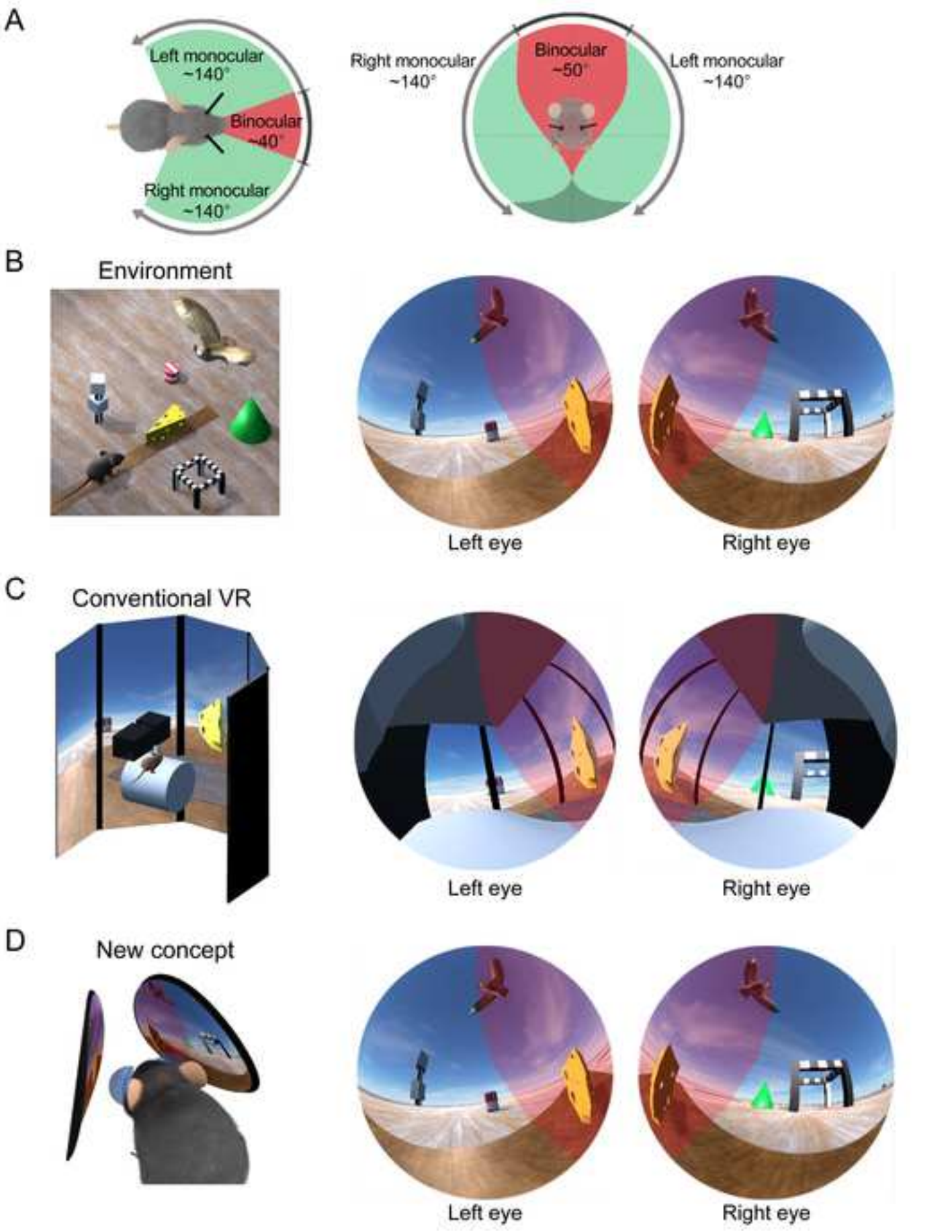

Figure 2

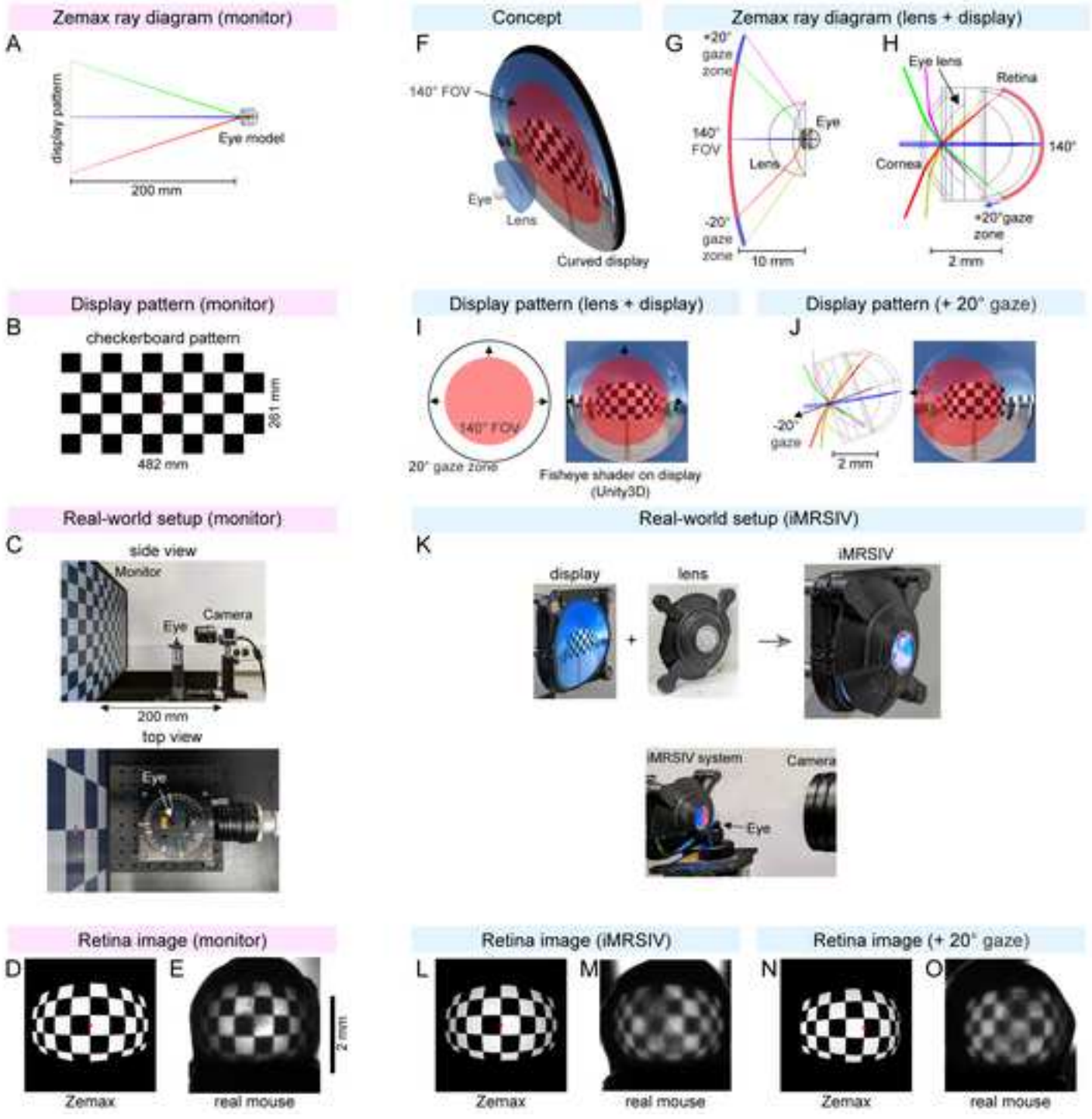

Figure 3

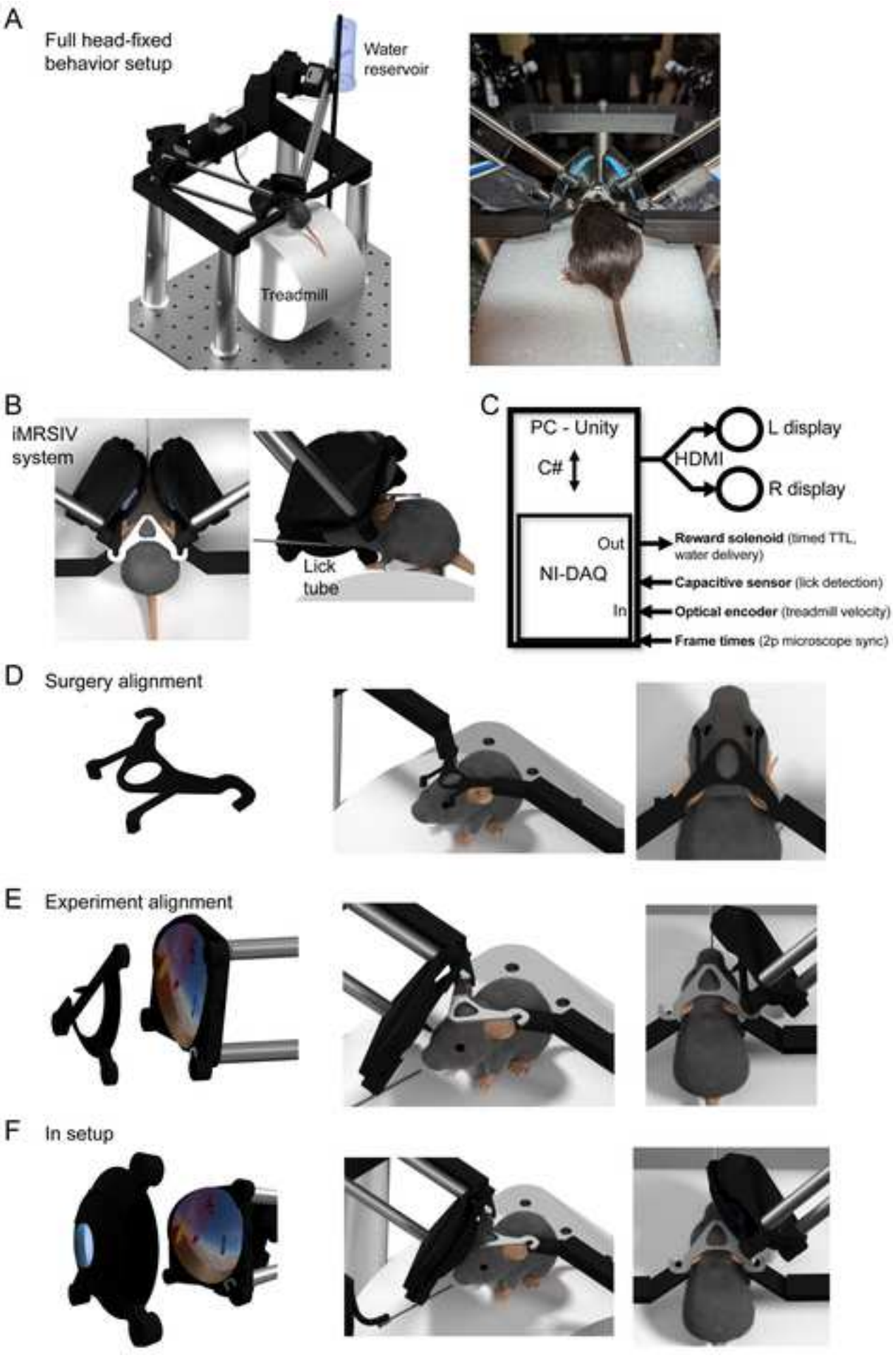

Figure 4

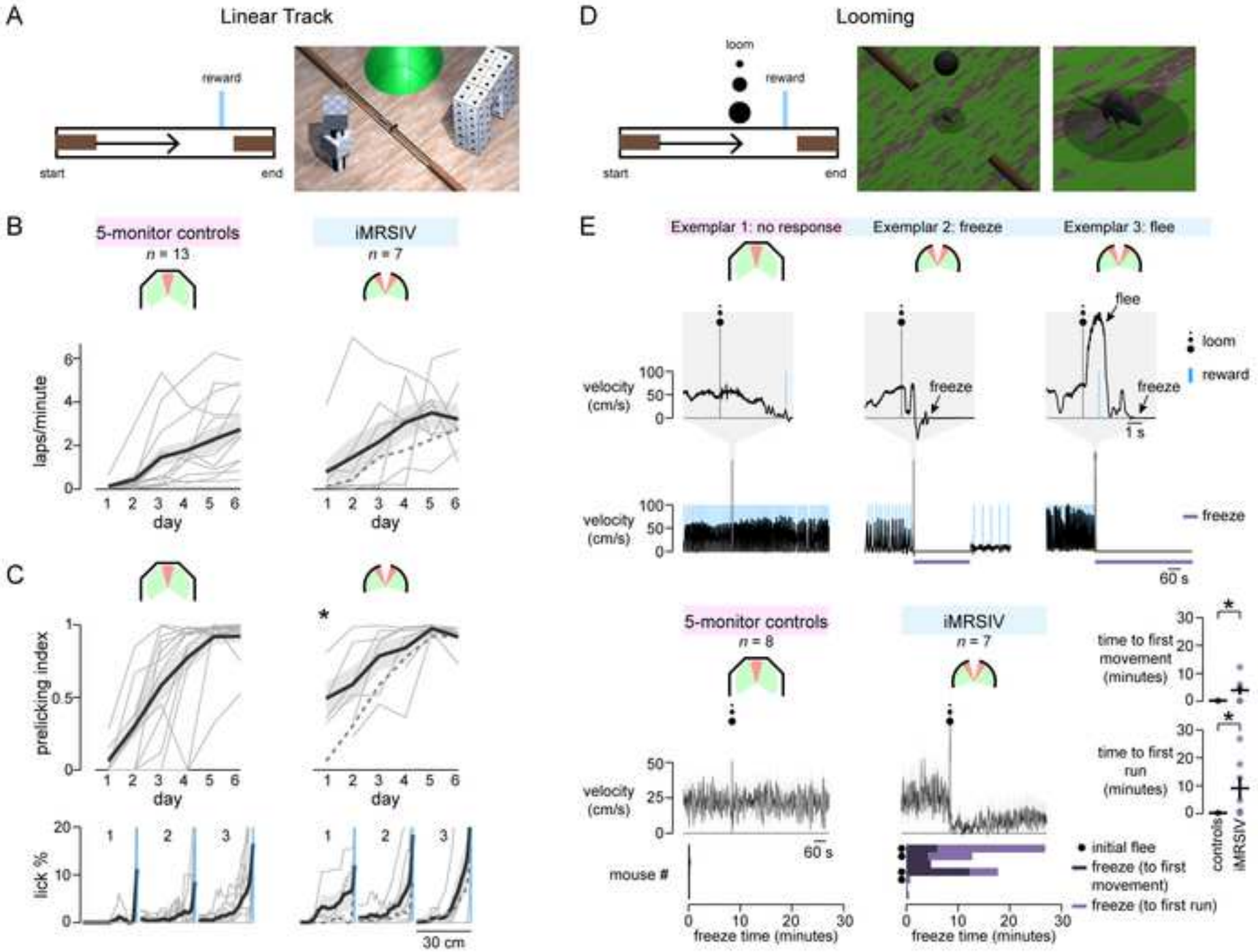

Figure 5

Click here to access/download;Figure;Fig_5.tif

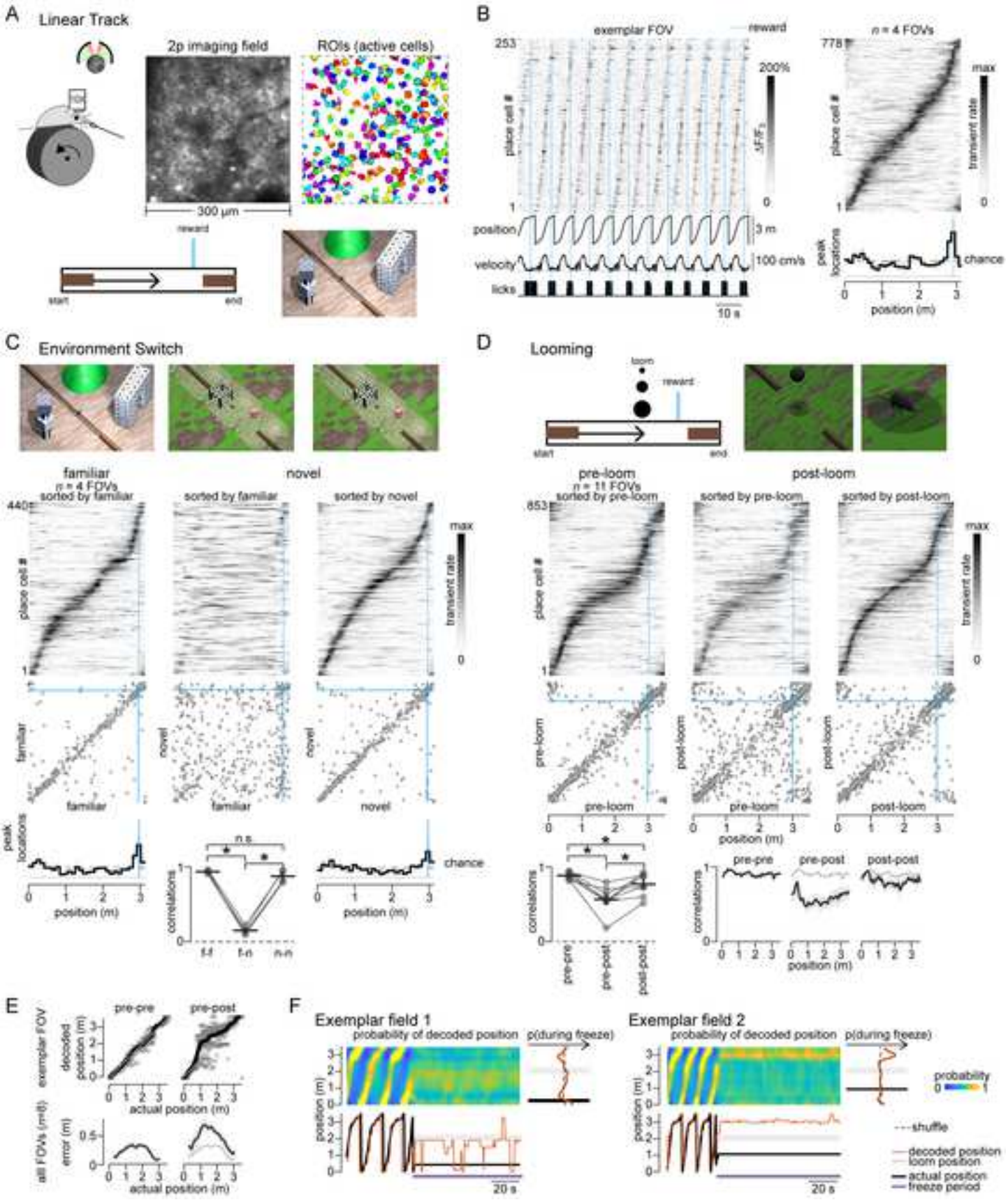

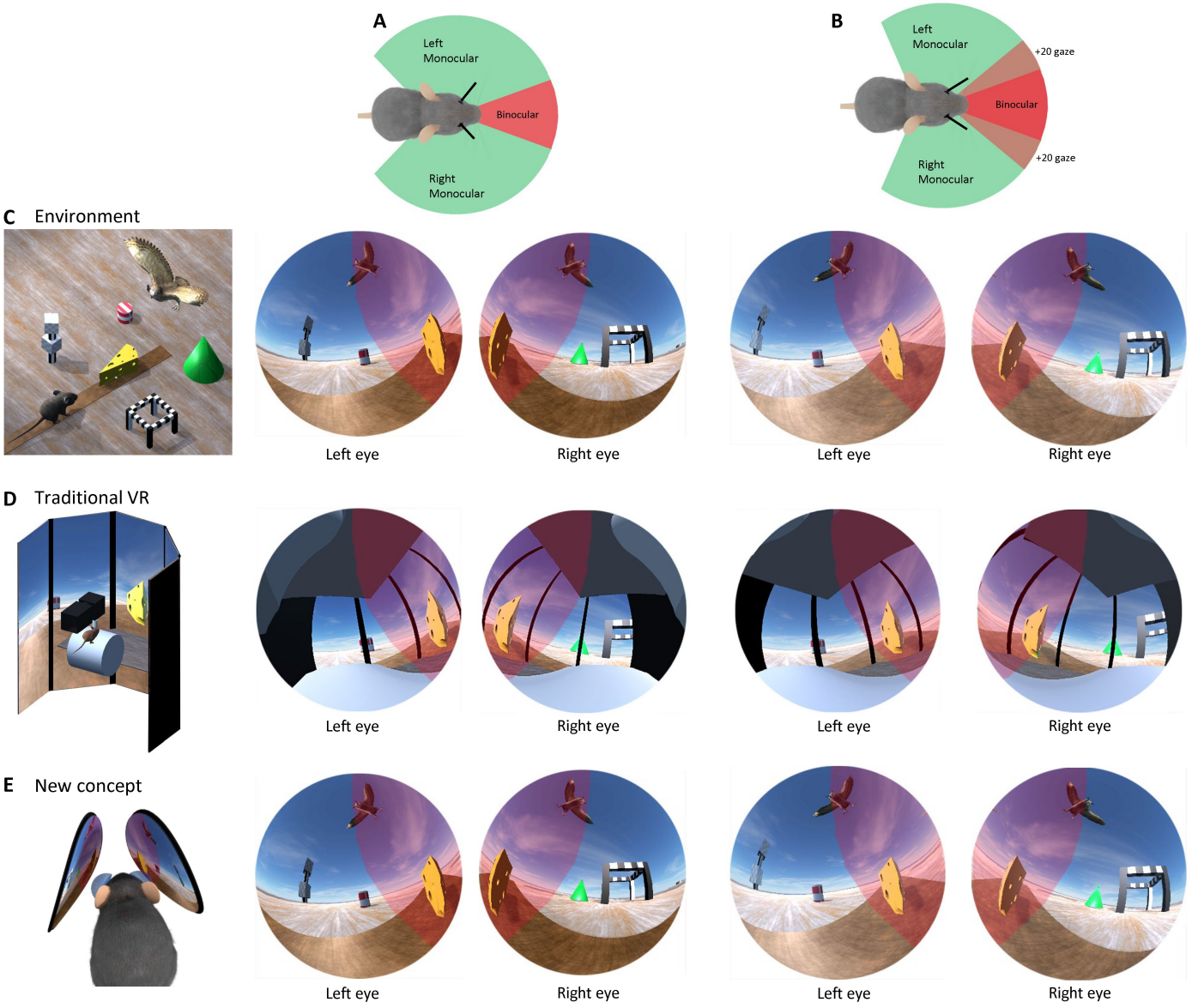

Figure S1. The mouse visual system and a new concept for mouse virtual reality goggles (20-degree saccade), related to Figure 1.
(A) Mouse visual field of view with monocular (green) and binocular (red) regions shown at resting eye gaze position from top-down and angled perspectives.
(B) Same as **(A)**, but with 20-degree forward saccade in both eyes; note expanded binocular zone.
(C-E) Columns 1, 2, 3 reproduced from Figure 1B-D. Columns 4,5 same as 2,3, but with 20-degree forward saccade in both eyes.

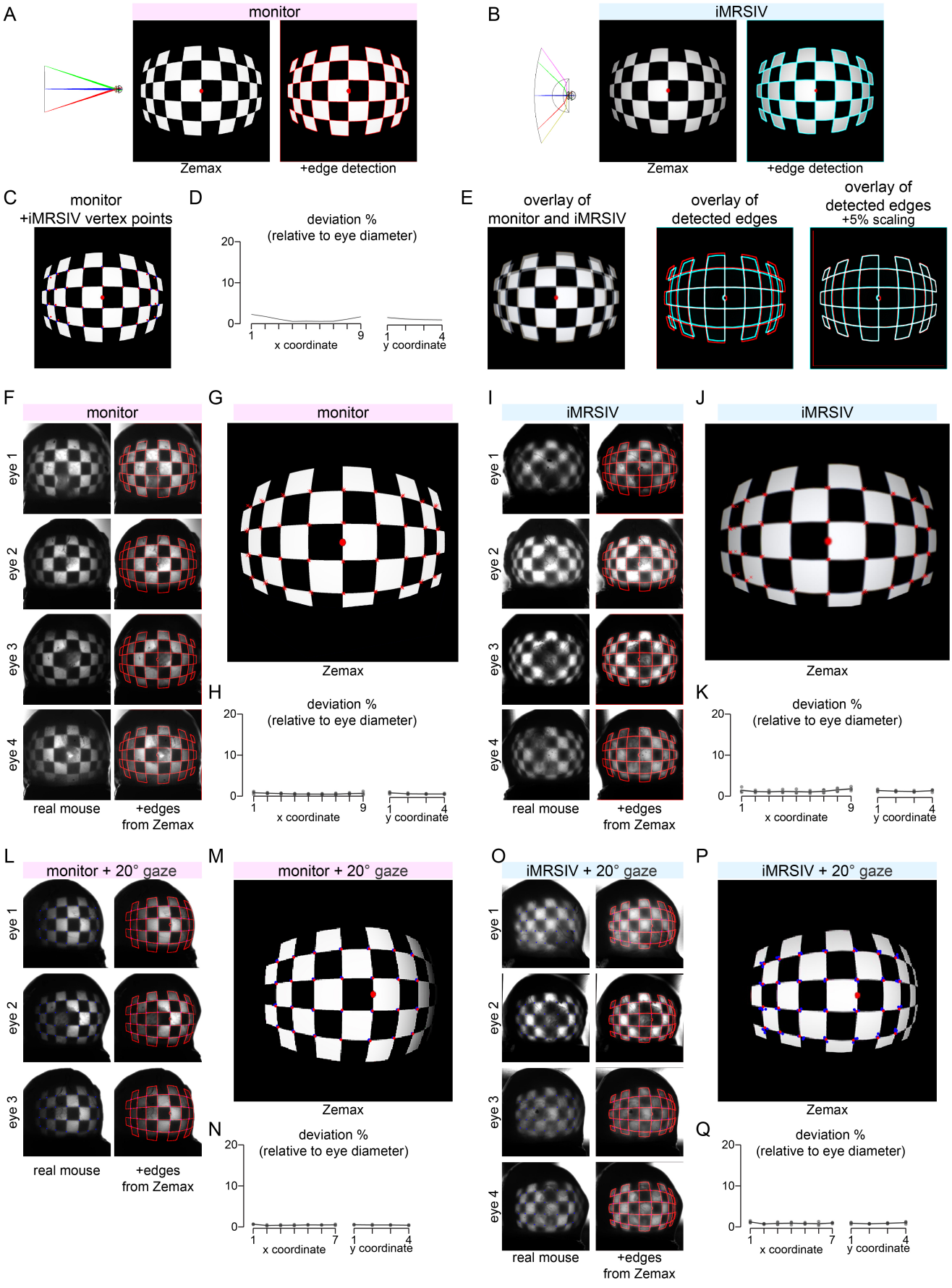
A
monitor
Zemax
+edge detection
B
iMRSIV
Zemax
+edge detection
C
monitor
+iMRSIV vertex points
D
deviation %
(relative to eye diameter)
20
10
0
1
9
x coordinate
1
4
y coordinate
E
overlay of
monitor and iMRSIV
overlay of
detected edges
overlay of
detected edges
+5% scaling
F
monitor
eye 1
eye 2
eye 3
eye 4
real mouse
+edges
from Zemax
G
monitor
Zemax
H
deviation %
(relative to eye diameter)
20
10
0
1
9
x coordinate
1
4
y coordinate
I
iMRSIV
eye 1
eye 2
eye 3
eye 4
real mouse
+edges
from Zemax
J
iMRSIV
Zemax
K
deviation %
(relative to eye diameter)
20
10
0
1
9
x coordinate
1
4
y coordinate
L
monitor + 20° gaze
eye 1
eye 2
eye 3
real mouse
+edges
from Zemax
M
monitor + 20° gaze
Zemax
N
deviation %
(relative to eye diameter)
20
10
0
1
7
x coordinate
1
4
y coordinate
O
iMRSIV + 20° gaze
eye 1
eye 2
eye 3
eye 4
real mouse
+edges
from Zemax
P
iMRSIV + 20° gaze
Zemax
Q
deviation %
(relative to eye diameter)
20
10
0
1
7
x coordinate
1
4
y coordinate

Figure S2. Quantification of similarity between Zemax and real mouse retinal projections for monitor and iMRSIV displays, related to Figure 2.

(A) Resulting image of the checkerboard object on the Zemax simulated eye retina with monitor at a distance of 200 mm, view from the back of the retina (same as Figure 2D). Edges of the checkerboard were detected and overlaid in red ('edge detection').

(B) Resulting image of the checkerboard object on the Zemax simulated eye retina with iMRSIV, view from the back of the retina (same as Figure 2L). Edges of the checkerboard were detected and overlaid in cyan ('edge detection').

(C) Vertex points were selected from the checkerboard on the Zemax-simulated retina images (monitor from panel **A**, red dots; iMRSIV from panel **B**, blue dots) and superimposed on the Zemax-simulated retina image with the monitor (from panel **A**).

(D) Deviation between vertices shown in **C**. The Cartesian distance between pairs of points is calculated and then normalized to the total diameter of the eye used in the model. These distances are then averaged over columns or rows of the checkerboard to attain deviation distance as a function of the x-axis or y-axis, respectively. As a coarse estimate, a 1% deviation corresponds to ~0.03 mm (eye diameter ~3 mm) or to ~1.4 degrees (eye diameter ~140 degrees), which is less than the mouse visual acuity of 0.375 cycles/degree (or 2.6 degrees/cycle).

(E) Superposition of Zemax-simulated retina images or detected edges from monitor (**A**) and from iMRSIV (**B**). Scaling the iMRSIV image by 5% (right) corrects for the slight magnification difference between the two optical systems.

(F) Image of the real world computer monitor checkerboard object on the retina of an extracted mouse eye (same as Figure 2E, but now shown across 4 separate eye experiments). After registering images to the Zemax simulated image (from **A**), vertex points were selected from the checkerboard images on the extracted eyes. Detected edges from Zemax simulated image superimposed as well to aid comparison.

(G) Vertex points (selected from real eye images in **F**) superimposed on the Zemax-simulated retina image with monitor.

(H) Deviations calculated for each of the 4 eye experiments. Each dot represents data from one eye; line and shading represent mean +/- SEM across the 4 eyes.

(I-K) Same as **F-H** but using iMRSIV (as in Figure 2L,M).

(L-Q) Same as **F-K** but with 20-degree gaze deviation (as in Figure 2J,N,O).

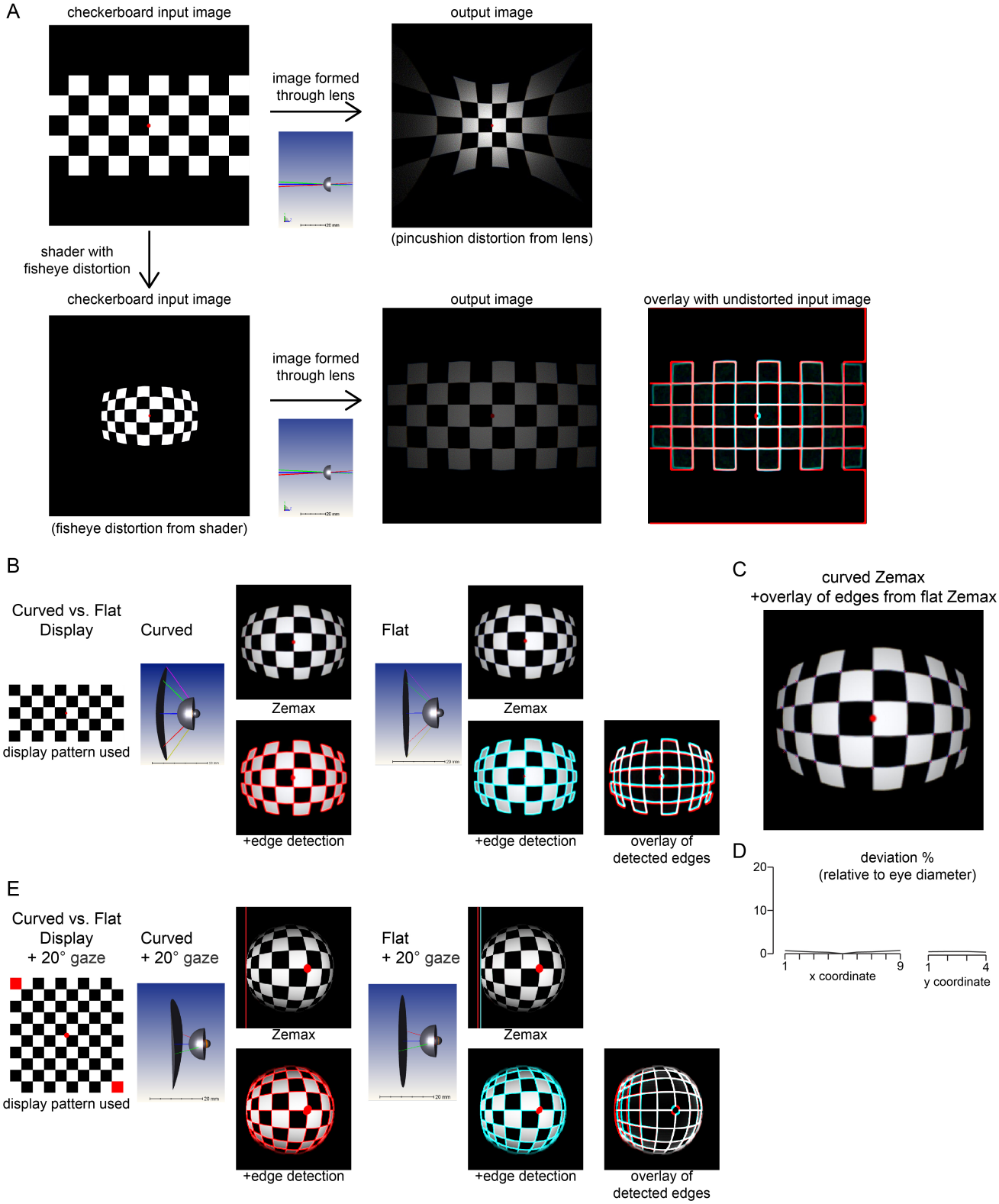

Figure S3. Optical details of the iMRSIV system, related to Figure 2 and STAR Methods.
(A) Fisheye shader in Unity used to generate large FOV and compensate for distortions of the iMRSIV lens. The iMRSIV lens that we used introduced a pincushion distortion (top row), as simulated using Zemax. Thus we first applied a fisheye distortion to the input image (bottom left); when that image is passed through the lens, as simulated in Zemax, the output image (represented with red in the overlay image) is now largely

undistorted (bottom right) and highly similar to the original checkerboard input image (represented with cyan in the overlay image).
(B-E) Curved vs non-curved side comparison. Due to mechanical limitations, we could only curve the screen along one axis (azimuthal). Here we used Zemax to simulate the images formed on the retina with and without curvature of the screen. Optically, distortions between the two axes were practically identical. However, along the curved axis, we achieved a slightly larger FOV. We chose the azimuthal axis because the mouse makes more frequent and larger saccades along this axis, but the curvature could easily be switched to the vertical direction if desired.
(B) Resulting image of the checkerboard object on the Zemax simulated eye retina with iMRSIV (with and without curvature), view from the back of the retina. Edges of the checkerboard were detected and overlaid in red or cyan ('edge detection'), respectively, and superimposed ('overlay of detected edges').
(C) Vertex points (selected from 'Curved' and 'Flat' images in **B**) superimposed on the Zemax-simulated retina image with the curved iMRSIV ('Curved' from **B**).
(D) Deviation between vertices shown in **C**. The Cartesian distance between pairs of points is calculated and then normalized to the total diameter of the eye used in the model. These distances are then averaged over columns or rows of the checkerboard to attain distance as a function of the x-axis or y-axis, respectively.
(E) Same as **B** but with 20-degree gaze deviation and a full square checkerboard as the display pattern. Edges detected from checkerboard are shown superimposed on the retina images and also each other ('overlay of detected edges'). The 'Curved' screen provides a slightly larger field of view; this is visualized by the vertical straight red and cyan lines, which delineate the edge of the image formed for the 'Curved' and 'Flat' configurations, respectively.

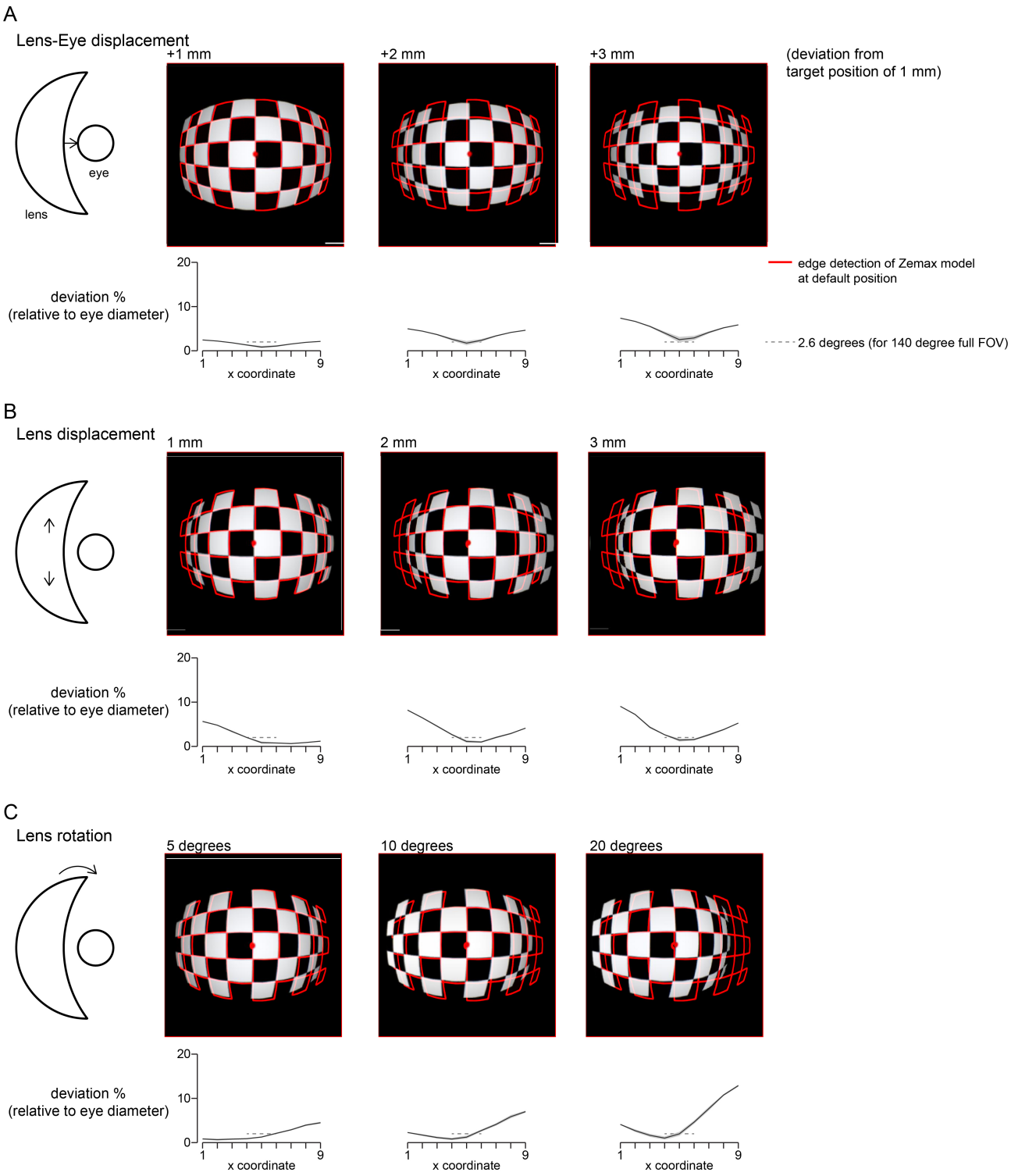

Figure S4. Optical distortions incurred by misalignment of iMRSIV system, related to Figure 3.
(A-C) We tested the distortions incurred by misalignment of the iMRSIV system relative to the eye using Zemax simulations. The default configuration is 1 mm of distance from the inner curve of the iMRSIV lens to the lens of the eye with no displacement or rotation. In each case, we altered the alignment along one dimension and acquired the Zemax-simulated retina image of the checkerboard pattern. We compared to (and superimposed) the retina image using the default configuration (as used in Figure 2L and Figure S2B) and quantified the deviations as a percentage of the eye diameter. As a coarse estimate, a 1% deviation corresponds to ~0.03 mm (eye diameter ~3 mm) or to ~1.4 degrees (eye diameter ~140 degrees), which is less than the mouse visual acuity of 0.375 cycles/degree (or 2.6 degrees/cycle).

(A) Lens-eye displacement (axial). The lens-eye distance was increased by +1 mm, +2 mm, or +3 mm from the default distance of 1 mm.
(B) Lens displacement (lateral). The iMRSIV lens was displaced relative to the eye position by 1 mm, 2 mm, or 3 mm.
(C) Lens rotation. The iMRSIV lens and display were together rotated relative to the axis of the eye and retina.

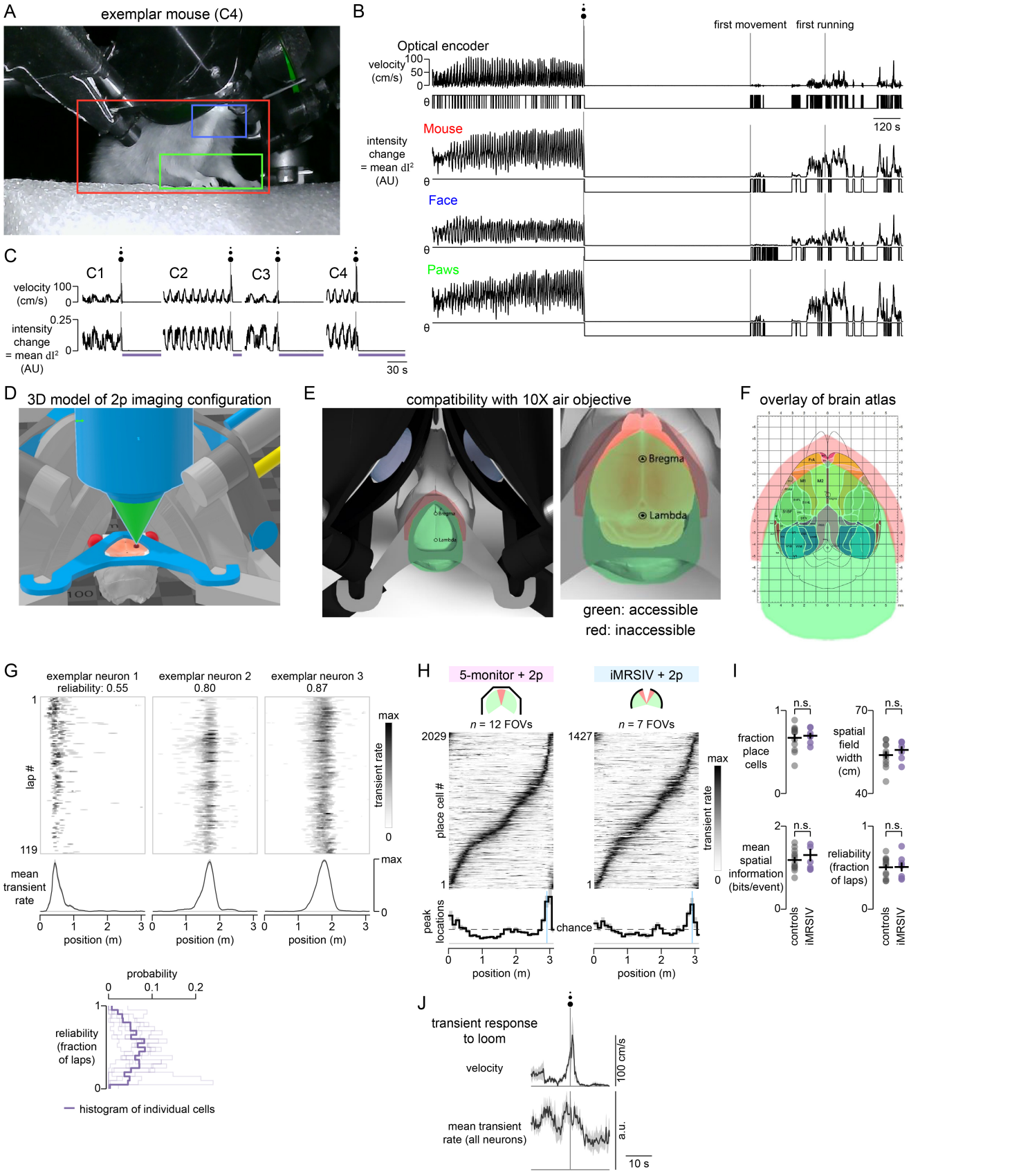

Figure S5. Additional detail on response to looming stimulus and two-photon imaging with iMRSIV, related to Figure 4 and Figure 5.
(A-C) Verification of freezing response to looming stimulus.

(A) Along with the treadmill velocity, we also took video of the mouse during presentation of a looming stimulus. We quantified any movement by measuring the energy averaged over pixels within an ROI (sum of the square of the time derivative at each pixel). This measure provided a sensitive means of detecting any motion of the mouse, even if the treadmill was not moved. Shown here is a single frame from the movie and three ROIs tested: 'Mouse' (red), which selected the whole body; 'Face' (blue), which selected the head/neck; and "Paws" (green), which selected the forelimbs.
(B) For the exemplar mouse ('C4') we plotted the treadmill velocity and the energy in each ROI over the course of the entire behavior session during which the loom was presented. Underneath each trace, we also plot a threshold indicator function that detects when the corresponding trace is different from zero. As can be appreciated from the plot, all measures are highly correlated. Importantly, in the time from the looming stimulus until the first movement, all channels show zero motion, verifying that the zero treadmill velocity reflects what is likely true freezing by the mouse (and not simply immobility).
(C) For four individual experiments, we show the treadmill velocity and the energy in the 'Mouse' whole-body ROI for a 2-minute span around the time of the loom.
(D-F) Cortical regions that are accessible with an overhead microscope and 10X objective.
(D) 3D model of the 2p imaging configuration, showing the mouse skull and eyes, head plate, iMRSIV lens and displays, and the position of the 10X objective and the cone of light centered above the position of CA1.
(E) Accessible (green) and inaccessible (red) regions of the dorsal surface of cortex using a standard overhead microscope and 10X objective with iMRSIV.
(F) Overlap of accessible-inaccessible regions along with a mouse brain atlas.
(G-J) Comparison of CA1 place cells in iMRSIV system to traditional 5-panel virtual reality.
(G) Lap-by-lap activity of three exemplar CA1 neurons during navigation in iMRSIV. Mean traces are shown underneath. Reliability score, defined as the fraction of laps with significant firing within the respective place field of each neuron, is indicated. Histogram (bottom inset) shows the distribution of reliability scores for all place cells across 7 imaging sessions using iMRSIV.
(H) Aggregate place cell data for all imaging sessions on the linear track (including familiar sessions and first part of track switch sessions when the track was familiar; the subset of these for only familiar sessions is shown in Figure 5B), for both traditional 5-monitor VR and iMRSIV. Mean transient rate vs. track position for all place cells from familiar environment imaging sessions (5-monitor controls: n=5 mice; iMRSIV: n=4 mice), even trial number firing patterns sorted based on place field location on odd trials, and histogram of place field peak locations underneath.
(I) Quantification of place cell characteristics using four different metrics. Fraction place cells: fraction of cells in a session that are place cells (see Methods). Spatial field width: length of track over which lap-averaged cell firing is greater than 30% of the max, applied to place cells only. Mean spatial information: spatial information score, applied to all cells. Reliability: fraction of laps with significant firing within the place field of that cell, applied to place cells only (see Methods). Each point represents the mean for all cells from one imaging session; black cross represents mean ± SEM across sessions. Statistical tests performed between 5-monitor controls and iMRSIV data (2-sample t-test).
(J) Population response to looming stimulation. The mean transient rate for a given imaging session was triggered on the time of the onset of the looming stimulus.

Supplemental Video 1

Click here to access/download

Supplemental Videos and Spreadsheets

Supplementary Movie 1.mp4

Supplemental Video 2

Click here to access/download

Supplemental Videos and Spreadsheets

Supplementary Movie 2.mp4

Supplemental Video 3

Click here to access/download

Supplemental Videos and Spreadsheets

Supplementary Movie 3.mp4